Journal of Fluids and Structures 124 (2024) 104047

Contents lists available at ScienceDirect

Journal of Fluids and Structures

journal homepage: www.elsevier.com/locate/jfs

Nonlinear shock-induced flutter of a compliant panel using a fully coupled fluid-thermal-structure interaction model

Al Shahriar, Kourosh Shoele *

Department of Mechanical Engineering, FAMU-FSU College of Engineering, 2525 Pottsdamer St., Tallahassee, 32310, FL, USA

ARTICLE INFO

Keywords:
Shock wave boundary layer interactions
Fluid–structural–thermal interactions
Fully-coupled simulation
Shock induced fluttering

ABSTRACT

A comprehensive study has been conducted on the fully coupled aero-thermo-elastic interaction between a shock wave and a laminar boundary layer over a flexible surface with different thermal conditions. In this investigation, the flow is characterized by an oblique impinging shock on a laminar boundary layer over a compliant panel with a cavity pressure and temperature. To model the fluid–structure interaction (FSI), we have combined a finite element model of the structure with a high-order sharp interface immersed boundary method implemented in a finite-difference flow solver. We have analyzed the behavior of the FSI coupling over a wide range of parameters and various boundary conditions while the panel undergoes relaxation to its unexcited state or exhibits limit cycle oscillations. Notably, the panel oscillation and the fluctuations in the shear layer exhibit strong coupling and demonstrate a lock-in resonance frequency response. The colder wall conditions result in a reduced separation bubble and a raised aerodynamic pressure difference between the maximum and minimum instantaneous dynamic pressures, consequently amplifying the amplitude of panel oscillation. For the cases with thermal coupling, the behavior of panel oscillation is notably influenced by specific heat and thermal expansion coefficients. In these scenarios, the thermal state of the solid material emerges as the pivotal factor governing the sustained oscillation of the panel. The non-linear impact of the thermal dependency of the structural properties plays a crucial role in determining the stability of the coupled FSI system. The study revealed that the stable decaying sinusoidal oscillation undergoes a transformation into a limit-cycle oscillation when panel stiffness is affected by reduced temperature. During the sustained oscillation, a mode switch is observed between the first and second modes of deformation of the panel.

1. Introduction

Shock wave boundary layer interaction (SBLI) is an intricate flow phenomenon encountered by airfoils operating at high speeds, control surfaces during supersonic/hypersonic flight, and high-speed engine inlets (Niessen, 2017; Délery and Dussauge, 2009; Dolling, 2001). The occurrence of SBLI over a compliant surface gives rise to various types of fluid–structure interaction (FSI) responses which are contingent upon the flexibility and thermal condition of the surface. The FSI phenomenon exhibits sensitivity to both boundary and initial conditions, necessitating the use of suitable computational methods and accurate implementation of boundary conditions for conducting a reliable numerical investigation (Bhardwaj and Mittal, 2012; Mittal et al., 2008; Dowell and Hall, 2001; Hou et al., 2012). Different complex flow and structural responses are associated with SBLI including unsteady behaviors, boundary layer separation, aerodynamic heat generation, buffeting/fluttering, and flow instabilities. The fundamental

* Corresponding author.
E-mail address: kshoele@fsu.edu (K. Shoele).

https://doi.org/10.1016/j.jfluidstructs.2023.104047
Received 28 July 2023; Received in revised form 6 November 2023; Accepted 7 December 2023
Available online 20 December 2023

Nomenclature

α	thermal diffusion, $\kappa/C_p\rho$
α_Δ	coefficient of thermal expansion
β	shock angle
$\boldsymbol{d}$	displacement of the solid
$\boldsymbol{f}$	body force component
$\boldsymbol{u}$	fluid velocity
δ	boundary layer thickness
ϵ	strain
γ	specific heat ratio
κ	thermal conductivity
λ	non-dimensional dynamic pressure, $\rho_\infty U^2 a^3/D$
λ_s	decay rate
$\boldsymbol{\sigma}$	viscous stress tensor
μ	dynamic viscosity
μ_M	Mach angle
ν	kinematic viscosity, μ/ρ
ν_s	Poisson ratio
ρ	density
σ_v	von Mises stress
$\mathbf{F}$	deformation gradient tensor
θ	deflection angle
a	panel length
C_a	Cauchy number, $\rho_\infty U^2/E$
C_{p_f}	specific heat of the fluid
C_{p_s}	specific heat of the solid
D	bending stiffness or flexural rigidity, $Eh^3/12(1-\nu_s^2)$
Ec	Eckert number
f	frequency
H	total enthalpy of the fluid
h	specific enthalpy
h_t	thickness of the panel
L_c	characteristic length
L_{sep}	length of separation
M^*	mass ratio, $\rho_f a/\rho_s h$
Ma	Mach number
P_c	cavity pressure
Pr	Prandtl Number, $\mu C_{p_f}/\kappa$
Re	Reynolds number, UL_c/ν
St	Strouhal number, fD/U
T_f	fluid temperature
U	incoming flow velocity
u, v, w	components of velocity
w, s, f, ∞	subscripts for wall, solid, fluid, and freestream
δ_i	identity tensor
$\boldsymbol{\sigma}_s$	Cauchy stress tensor
b	body force
E	Young's modulus
K	material stiffness
Q	heat generation
q	heat flux

flow behaviors and physics of SBLI are usually studied within two canonical configurations: (1) flow over the compression ramp and (2) the incident oblique shock on the boundary layer over a flat surface. These two systems share many similarities, such as the formation of separation bubbles, downstream thickening of the boundary layer, high peak heating, unsteadiness, and dependence on

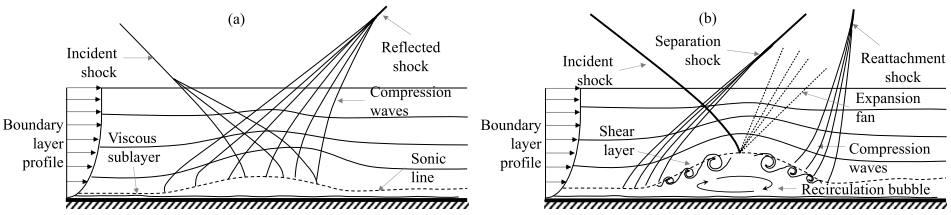

Fig. 1. Schematics of the shock reflection from a rigid surface (a) without boundary layer separation (Délery and Dussauge, 2009), (b) with boundary layer separation (Pasquariello et al., 2014).

the properties of the incident flow. For both configurations, there is extensive research that characterizes the role of SBLI over rigid structures using numerical and experimental approaches. These include the flow physics of laminar (Pagella et al., 2002; Benay et al., 2006; Robinet, 2007; Guiho et al., 2016; Gs et al., 2017; Shahriar et al., 2018), turbulent (Sansica et al., 2014; Ganapathisubramani et al., 2007; Wu and Martin, 2007; Délery and Dussauge, 2009; Touber and Sandham, 2009; Nichols et al., 2017; Priebe and Martín, 2012; Piponniau et al., 2009; Pirozzoli and Grasso, 2006), and transitional (Sandham et al., 2014; Shinde et al., 2018) boundary layers interactions. The numerical studies have utilized techniques such as large eddy simulation (LES) (Agostini et al., 2012; Aubard et al., 2013; Grilli et al., 2012; Touber and Sandham, 2009; Garnier, 2009) and direct numerical simulation (DNS) (Fang et al., 2014; Pirozzoli and Grasso, 2006; Wu and Martin, 2008).

The principal characteristics of SBLI have been well-documented in the literature (Babinsky and Harvey, 2011; Dolling, 2001). The impinging SBLI problem has two distinct flow structures, as shown in Fig. 1, depending on the strength of the shock (pressure jump across the shock). For a comparatively weaker shock (i.e., a small pressure jump across the shock), the boundary layer experiences a moderate adverse pressure gradient and the consequences on the boundary layer are insignificant. On the other hand, for a stronger shock, the boundary layer experiences a large adverse pressure gradient and consequently, the boundary layer undergoes separation and creates a recirculation bubble. In comparison with the turbulent SBLI, the separation bubble can be generated by a relatively weaker shock and the size of the interaction zone is larger for laminar SBLI (Babinsky and Harvey, 2011; Robinet, 2007).

The thermal wall condition has a significant impact on the characteristic scales of SBLI and several studies have employed computational methods and experiments to investigate SBLI over non-adiabatic surfaces (Bernardini et al., 2016; Jaunet et al., 2014; Hayashi et al., 1986). In the experimental study by Jaunet et al. (2014), it was observed that the wall heating effect significantly impacted the size of the interaction region and the low-frequency unsteadiness. The heat transfer coefficient exhibits three distinct changes along the wall with a sharp increase near the reattachment and separation points of the bubble (Hayashi et al., 1986). Strong cooling can delay the onset of the laminar-turbulent boundary layer transition (Delery, 1985) and the wall cooling can reduce the characteristic lengths of the interaction (Bernardini et al., 2016). Cooling of the boundary also reduces the sensitivity of SBLI to upstream condition (Shinde et al., 2018; Dolling, 2001), and facilitates the flow recovery downstream of SBLI region (Priebe and Martín, 2012). Volpiani et al. (2018, 2020) have conducted numerical investigations on turbulent SBLI in both supersonic and hypersonic regimes over the rigid wall for different non-adiabatic wall conditions where they observed that the wall temperature has a considerable effect on the size of the interaction region and pressure fluctuations. It was found that the interaction length scales depend more on the shock strength or wall cooling than on the Reynolds number. However, an interesting observation was that the smaller interaction region for the cooled wall leads to maximum thermal and dynamic loads locally. This could change the dynamic aerodynamic forces that the flexible panel senses and as a result, there could be a significant change in the flow-induced vibration of the flexible surfaces depending on the thermal condition of the boundary. Studying such interconnecting effects of surface flexibility and thermal conditions is the main objective of this paper.

The presence of a compliant interface also plays an important role in the dynamics of the boundary layer for high-speed flows. The aeroelastic behavior of high-speed flow is usually examined with the canonical problem of panel flutter (Ostoich et al., 2013; Vedeneev, 2012; Sander et al., 1973). Ostoich et al. (2013) observed that the unstable eigenmodes of the initial laminar boundary layer flow become stronger in time due to the panel motion and further lead to oscillating shocks. The fluid–structure interaction (FSI) with the presence of SBLI is substantially more complex (Visbal, 2012, 2014; Willems et al., 2013; Hosters et al., 2013). It encloses a strong correlation between shock strength and the amplitude and frequency of the panel oscillation, which itself triggers unsteady responses of the expansion fan, reattachment, and reflected shocks (Visbal, 2012, 2014). In the experiments conducted by Willems et al. (2013), it was seen that the reflection of the incoming shock and characteristics of the separation bubble is affected by the panel deflection. The structural deflection consists of a large static deflection and small amplitude vibrations. The static deflection of the panel is proportional to the mean pressure of the flow. Brouwer et al. (2017) observed that although the unsteady deformation brings changes to the length and size of the separation bubble, it is the static surface deformation that can substantially increase or decrease the bubble length. They proposed that the surface curvature and surface velocity modify the separation on the interface. Recently, Shinde et al. (2018) showed that the average length of the bubble is smaller for a flexible panel compared to a rigid panel. The mean wall pressure of the flexible panel was found to be lower near the separation and higher near the reattachment regions compared to the rigid panel. Different levels of panel vibration induce certain compression and expansion waves while, at the same time, these waves increase the role of shocks on FSI responses (Pasquariello, 2018).

The structural non-linearity associated with the coupling between bending and stretching of the panel has been represented as a manifestation of the increased modal frequencies of the panel deflection (Shinde et al., 2022). In an experimental study by D'Aguanno et al. (2023), the regions that have the maximum correlation between the displacement and the flow velocity fluctuations have been identified and a match has been found between the primary frequency in the panel's oscillation and the primary spectral components of the reflected shock wave. In a weakly coupled FSI system, when the panel oscillation amplitude is very small, the pressure fluctuations demonstrate discrete peaks for the frequencies close to the panel resonance mode frequencies without any changes in the mean separation size (Varigonda and Narayanaswamy, 2023). The panel flexibility, shock impingement strength, and location can shift the characteristic aeroelastic behavior from a structurally dominated to a fluid-dominated system where the oscillations are sustained by either the incoming flow fluctuations or the fluid–structure coupling (Vasconcelos et al., 2023). Zhou et al. (2023) reported that shock impingement location and cavity pressure are responsible for the transition between a subcritical bifurcation and a supercritical bifurcation of a coupled shock-induced aeroelastic FSI system. Freydin et al. (2022) investigated the aeroelastic response of a plate subjected to turbulent SBLI, where they analyzed the experimental pressure field, specifically investigating local mean, root mean square (RMS), and spatial coherence length. Subsequently, this characterized pressure field was utilized to model the fluid–structure response. Empirical observations from their study show that the boundary layer thickness plays a significant role in the excitation process. In a recent examination of turbulent SBLI over a flexible panel, the researchers noted a notable increase in pressure variation amplitude compared to a rigid panel. Additionally, alterations in the size and configuration of the separation zone resulted in a distinct distribution of skin-friction coefficients. This led to the proposition that a new low-frequency flow unsteady response, equivalent in magnitude to the vibration of the elastic panel, has emerged (Gao et al., 2023).

There has been much less research on the thermo-elastic response at high-speed flows, despite its key role in fatigue damages at high-speed flows (Spottswood et al., 2019; Thornton, 1992). The response of a plate with temperature-dependent material properties inside high-speed flow without shock was studied experimentally and represented with low-fidelity simulations where a good agreement was found (Freydin et al., 2021). In a recent experiment at Mach number of 5.33, a strong coupling was seen between the flow and the panel oscillation in which a large dependency on the temperature change in the flow was observed (Daub et al., 2022). Here, substantial surface heating modified the stiffness of the panel and, consequently, changed the panel's dynamic responses. Gaitonde and Adler (2022) pointed out that the amplification of any frequencies smaller than that of the turbulent boundary layer may assist FSI. The thermal wall boundary conditions will complicate the FSI system since SBLI yields significant localized heating and large wall-temperature gradients.

Most of the studies on impinging shock interactions with the boundary layer concentrate solely either on the dynamic aspects of the FSI system or primarily look at thermal effects on the separation characteristics of rigid walls, leaving a gap in our comprehensive understanding of coupled thermal and structural effects. Understanding the combination of thermal coupling and FSI interaction is a difficult task as it involves a wide range of scales including fluid and solid instabilities and thermal transport dynamics. If the dominant timescale of the flexible surface is similar to the low-frequency oscillation of the separation bubble, the temperature variation in the panel could strongly affect the nonlinear interaction between the structure and fluid. Previous research on the thermo-elastic response in high-speed flows has predominantly leaned towards experimental endeavors. Theoretical investigations, on the other hand, have been limited and primarily rely on either analytical methods or a combination of numerical and analytical approaches (Culler and McNamara, 2011, 2010; Culler, 2010; Purwar et al., 2017). Nevertheless, in most of these approaches, the underlying physics are somewhat simplified. Still, there is no comprehensive understanding of SBLI that can pinpoint the destructive and constructive interactions between FSI, shock dynamics, and the thermal condition of the panel (Shahriar et al., 2018). In this study, we investigate the interaction between shockwaves and flexible surfaces with varying thermal properties, underscoring the critical role of thermo-elastic coupling in SBLI over flexible surfaces.

The rest of the paper is organized as follows. First, the numerical methodology and the problem setup are presented in Section 2. The initial conditions and boundary conditions along with interface conditions are discussed in Sections 2.3 and 2.4. The results for SBLI over the compliance surface for a dynamically coupled system are presented in Section 3.1. The fully coupled (both dynamically and thermally coupled system) interactions are discussed in Section 3.2. Finally, the conclusions and further directions are provided in Section 4.

2. Numerical method

In this study, a finite-difference flow solver is coupled with a finite-element thermal–structural solver using the partitioned coupling approach (Heil et al., 2008). In the current solution algorithm, at first, the flow field solution is obtained for the current thermal and kinematic conditions at the fluid–solid interface. The thermal and dynamic load acting on the interface are computed by adopting the high-order immersed boundary method (IBM) formulation (Seo and Mittal, 2011). The detailed formulation of the IBM method is presented in Appendix A. Following the determination of flow quantities at the interface, along with the current thermal and dynamic boundary conditions, dynamic deformation of the solid along with its thermal and response are calculated iteratively as a strongly coupled nonlinear system of equations until a convergence criterion is met (as described in Section 2.2.1). Once the thermal and dynamic state of the solid is determined, the updated kinematic and thermal conditions are transferred to the flow solver to start the new time step. The whole solution procedure is shown in Fig. 2 in a simplified manner. The main aspects and the governing equations of the flow and thermal/structural solver will be discussed briefly in the following sections, while the validations of the flow solver, structural solvers, and the coupling algorithm are given in Appendix B.

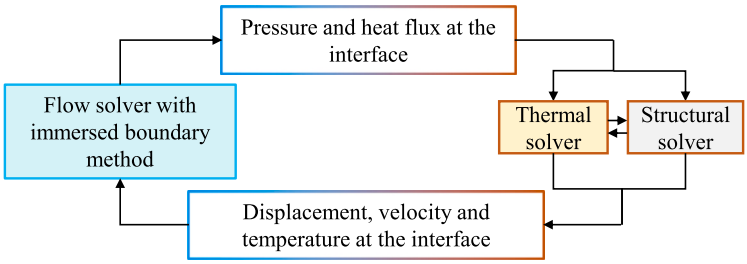

Fig. 2. Fluid–thermal–structure interaction (FTSI) algorithm.

2.1. Flow solver

The flow equations are nondimensionalized using the characteristic length a (length of the flexible panel), the characteristic velocity U (the free-stream velocity), characteristic temperature T_∞, pressure P_∞ and density ρ_∞ (based on the free stream condition and related by $P_\infty = \rho_\infty R T_\infty$), and free-stream viscosity μ_∞ and conductivity κ_∞.

$$\tilde{\boldsymbol{x}} = \frac{\boldsymbol{x}}{a}, \qquad \tilde{t} = \frac{t}{a/U}, \qquad \tilde{\rho} = \frac{\rho}{\rho_\infty}, \qquad \tilde{\boldsymbol{u}} = \frac{\boldsymbol{u}}{U}, \qquad \tilde{p} = \frac{p}{\rho_\infty U^2}, \tag{1}$$

$$\tilde{T} = \frac{T}{T_\infty}, \qquad \tilde{E} = \frac{E}{U^2}, \qquad \tilde{\mu} = \frac{\mu}{\mu_\infty}, \qquad \tilde{\kappa} = \frac{\kappa}{\kappa_\infty}, \tag{2}$$

where, $\rho, \boldsymbol{u}, p, T, E, \mu,$ and κ are the density, velocity vector, pressure, temperature, total energy, viscosity, and thermal conductivity respectively. In order to simplify the notation, the non-dimensional symbol ($\sim$) will be dropped out hereafter. This results in the following non-dimensional equations describing the conservation of mass, momentum, and total energy for the compressible calorically perfect gas flow,

$$\frac{\partial \rho}{\partial t} + \boldsymbol{\nabla} \cdot (\rho \boldsymbol{u}) = 0, \tag{3}$$

$$\frac{\partial (\rho \boldsymbol{u})}{\partial t} + \boldsymbol{\nabla} \cdot \left[\rho \boldsymbol{u} \otimes \boldsymbol{u} + p \mathbf{I} - \frac{1}{\mathrm{Re}} \boldsymbol{\sigma}_f \right] = 0, \tag{4}$$

$$\frac{\partial (\rho E)}{\partial t} + \boldsymbol{\nabla} \cdot \left[(\rho E + p)\, \boldsymbol{u} - \frac{1}{\mathrm{Re}} (\boldsymbol{\sigma}_f \odot \boldsymbol{u}) - \frac{1}{\mathrm{Re}\,\mathrm{Pr}\,(\gamma - 1)\,\mathrm{Ma}} \boldsymbol{q} \right] = 0, \tag{5}$$

where $\gamma = C_{p_f}/c_v$ is the specific heat ratio. The non-dimensional numbers that appeared in the above equations are Mach number (Ma), Reynolds number (Re), and Prandtl number (Pr) defined as

$$\mathrm{Ma} = \frac{U}{c_\infty}, \qquad \mathrm{Re} = \frac{\rho_\infty U\, a}{\mu_\infty}, \qquad \mathrm{Pr} = \frac{\mu_\infty c_{p,\infty}}{\kappa_\infty} \tag{6}$$

The non-dimensional total energy (E) per unit mass and the non-dimensional equation of state are defined as,

$$E = \frac{p}{\rho(\gamma - 1)} + \frac{1}{2} \boldsymbol{u} \cdot \boldsymbol{u}, \qquad p = \frac{1}{\gamma M a_\infty^2} \rho T, \tag{7}$$

and the viscous stress tensor ($\boldsymbol{\sigma}_f$) and the heat flux ($\boldsymbol{q}$) are,

$$\begin{aligned} \boldsymbol{\sigma}_f &= 2\left(\mu + \mu^*\right) \mathbf{S} + \left(\beta^* - \frac{2}{3}\right) (\boldsymbol{\nabla} \cdot \boldsymbol{u}) \mathbf{I}, \\ \boldsymbol{q} &= -\left(\kappa + \kappa^*\right) \boldsymbol{\nabla} T, \end{aligned} \tag{8}$$

where the strain rate tensor is,

$$\mathbf{S} = \frac{1}{2} \left[\boldsymbol{\nabla} \otimes \boldsymbol{u} + (\boldsymbol{\nabla} \otimes \boldsymbol{u})^T \right] \tag{9}$$

Here, μ and κ are the scaled dynamic viscosity and thermal conductivity, defined based on the well-known Sutherland's formula (Chapman and Cowling, 1990). In addition, μ^*, β^* and κ^* are the artificial shear viscosity, artificial bulk viscosity, and artificial thermal diffusivity defined on a non-uniform Cartesian grid as (Cook and Cabot, 2005, 2004; Fiorina and Lele, 2007; Kawai and Lele, 2007),

$$\begin{aligned} \mu^* &= C_\mu\, \rho \overline{|\boldsymbol{\nabla}^4 \mathbf{S}| \Delta^6}, \quad \beta^* = C_\beta\, \rho \overline{|\boldsymbol{\nabla}^4 \mathbf{S}| \Delta^6}, \\ \kappa^* &= C_\kappa \frac{\rho\, c}{T} \overline{\left| \boldsymbol{\nabla}^4 \left(\frac{RT}{\gamma - 2} \right) \right| \Delta^5} \end{aligned} \tag{10}$$

where Δ is the grid spacing. The over-bar denotes an approximate truncated Gaussian filter. Here, $C_\mu = 0.002$, $C_\beta = 1.0$, and $C_\kappa = 0.01$ is used, as suggested by Kawai and Lele (2007), and the fourth derivatives are computed by the central compact scheme (Lele, 1992).

A sixth-order compact central finite difference scheme and a third-order total variation diminishing Runge–Kutta (RK3-TVD) method are used for spatial and temporal discretizations of the flow equations, respectively (Lele, 1992; Bhardwaj et al., 2014; Bhardwaj and Mittal, 2012; Gottlieb and Shu, 1998).

2.2. Solid solver

To account for the geometric non-linearity, temperature dependency, and large deformation, the Green–Lagrangian strain tensor ($\mathbf{E}$) and second Piola–Kirchhoff stress tensor ($\mathbf{S}$) are used to express the stress–strain relationships.

$$\mathbf{S} = \mathbf{C} : \mathbf{E}_e, \qquad \mathbf{E}_e = \mathbf{E} - \mathbf{E}_T, \qquad \mathbf{E} = \frac{1}{2}(\mathbf{F}^T\mathbf{F} - \mathbf{I}) \tag{11}$$

where, ':' represents the double dot tensor product, $\mathbf{F}$ is the deformation gradient between the initial position and the current position, and $\mathbf{C}$ is the elasticity/stiffness tensor which is a function of Young's modulus and Poisson ratio. To account for the temperature dependency of the shear and strain, the thermal elasticity ($\mathbf{E}_T$) is considered, which can be described by the following equation under the assumption that thermal strain is minimal compared to the strain due to the external loading, as

$$\mathbf{E}_T = \alpha(T - T_{\text{ref}}) \tag{12}$$

where α is the coefficient of thermal isotropic expansion and T_{ref} is the stress-free temperature, chosen to be the same as the recovery temperature in the present study. The internal damping of the panel is assumed to be zero.

In the solid region, the non-dimensional unsteady equation of motion of a deformable solid body is written based on the Cauchy number (C_a) and the mass number (M^*) as,

$$\frac{d^2\boldsymbol{d}}{dt^2} = \frac{M^*}{C_a}\nabla\cdot\boldsymbol{\sigma}_s + \boldsymbol{f}_s, \quad C_a = \frac{\rho_\infty U^2}{E}, \quad M^* = \frac{\rho_\infty}{\rho_s} \tag{13}$$

where, $\boldsymbol{\sigma}_s$ is the nondimentional Cauchy stress tensor, E is the Young's modulus of the solid material and $\boldsymbol{f}_s$ is the nondimentional body forces per unit mass. Similarly, the transient heat conduction problem in the compliant body is represented by the local heat balance equation as,

$$c_V\frac{\partial T_s}{\partial t} + \nabla\cdot\boldsymbol{q}_s - Q = 0 \tag{14}$$

where c_V is a characteristic property of a solid material and Q is the heat generation rate per unit volume of the solid (in the current model $Q = 0$). In addition, the heat generation due to deformation, compression, or expansion is expected to be insignificant for the range of stress variations anticipated in this study and hence is not accounted for here. The heat flux ($\boldsymbol{q}_s$) is governed by Fourier law, $\boldsymbol{q}_s = -\kappa(\nabla T_s)$, where κ is 3×3 generalized thermal conductivity matrix. The unsteady heat conduction equation above is discretized and solved by a linear finite element and a trapezoidal time integration scheme.

The governing equations of motions are solved by the Galerkin finite-element method (FEM) where the finite element discretization yields the following system of ordinary differential equations for the nodal displacement $\boldsymbol{X}$, at the time step n,

$$\mathbf{M}\ddot{\boldsymbol{X}} + \mathbf{C}\dot{\boldsymbol{X}} + \boldsymbol{R}(\boldsymbol{X}) = \mathbf{F} \tag{15}$$

where, $\mathbf{M}$&$\mathbf{C}$ are coefficient matrices and $\boldsymbol{R}(\boldsymbol{X})$ is the geometrically nonlinear stiffness term. The Hilber–Hughes–Taylor (HHT) time integration scheme (Hilber et al., 1977) is used for temporal discretization. If $\boldsymbol{A}_n, \boldsymbol{V}_n$, and $\boldsymbol{D}_n$ are the approximations of $\ddot{\boldsymbol{X}}(t_n), \dot{\boldsymbol{X}}(t_n)$ and $\boldsymbol{X}(t_n)$, it can be written that

$$\begin{aligned}\boldsymbol{D}_{n+1} &= \boldsymbol{D}_n + \Delta t\boldsymbol{V}_n + \Delta t^2\left[(\frac{1}{2}-\beta)\boldsymbol{A}_n + \beta\boldsymbol{A}_{n+1}\right]\\ \boldsymbol{V}_{n+1} &= \boldsymbol{V}_n + \Delta t\left[(1-\gamma)\boldsymbol{A}_n + \gamma\boldsymbol{A}_{n+1}\right]\end{aligned} \tag{16}$$

and a one-step approximation to Eq. (15) can be formed as

$$\mathbf{M}\boldsymbol{A}_{n+1} + \mathbf{C}\boldsymbol{V}_{n+1-\alpha_f} + \boldsymbol{R}(\boldsymbol{D})_{n+1-\alpha_f} = \boldsymbol{F}(t_{n+1-\alpha_f}) \tag{17}$$

where,

$$\begin{aligned}t_{n+1-\alpha_f} &= (1-\alpha_f)t_n + \alpha_f t_{n+1}\\ \boldsymbol{R}_{n+1-\alpha_f} &= (1-\alpha_f)\boldsymbol{R}_n + \alpha_f\boldsymbol{R}_{n+1}\\ \boldsymbol{V}_{n+1-\alpha_f} &= (1-\alpha_f)\boldsymbol{V}_n + \alpha_f\boldsymbol{V}_{n+1}\end{aligned} \tag{18}$$

The coefficients are selected to reach an unconditionally stable and second-order accurate prediction while allowing the energy dissipation of high wave-number modes. In particular, α, β and γ are selected as $\alpha \in [-1/3, 0]$, $\gamma \in (1-2\alpha)/2$ and $\beta \in (1-\alpha)^2/4$.

2.2.1. Coupling algorithm between thermal and structural solver

In the coupling strategy established for the structural solver, the two material models were considered: (1) the heat transfer model and (2) the structural mechanics model. The solutions are obtained through an iterative algorithm where the heat transfer model first solves the temperature field of the beam and then the structural mechanics model solves for the deformation using the predicted material temperature until the residuals satisfy the convergence criterion. The whole physical system works under the assumption that the structure may experience thermal-induced stress but the temperature field will not be impacted by the deformation i.e. the heat generation due to continuous rapid deformation is negligible.

2.3. Boundary and interface conditions

2.3.1. Inflow conditions

The following steady compressible boundary layer equations, describing the flow of a compressible fluid near a solid surface in x-direction, were solved by the implicit finite difference method described in (White and Corfield, 2006).

$$\rho\left(u\frac{\partial u}{\partial x}+v\frac{\partial u}{\partial y}\right)=\frac{\partial v}{\partial y}\frac{\partial u}{\partial y}+\nu\frac{\partial^2 u}{\partial y^2} \tag{19}$$

$$\rho C_{p_f}\left(u\frac{\partial T}{\partial x}+v\frac{\partial T}{\partial y}\right)=\nu\left(\frac{\partial u}{\partial y}\right)^2+\frac{\partial k}{\partial y}\frac{\partial T}{\partial y}+k\frac{\partial^2 T}{\partial y^2} \tag{20}$$

where, T is the temperature, C_{p_f} is the specific heat at constant pressure, and k is the thermal conductivity. The evaluated solutions are imposed as inflow conditions during the simulation.

2.3.2. Shock generation

A shock wave is generated at the top boundary based on the Rankine–Hugoniot jump condition and the pressure and density of the flow are specified at the top boundary according to

$$\frac{p_2}{p_\infty}=1+\frac{2\gamma}{\gamma+1}\left((Ma\,\sin\beta)^2-1\right),\quad \frac{\rho_2}{\rho_\infty}=\frac{(\gamma+1)(Ma\,\sin\beta)^2}{(\gamma-1)(Ma\,\sin\beta)^2+2} \tag{21}$$

where β is the shock angle (the angle between the shock wave and the direction of the incoming flow) and Ma is the Mach number of the incoming flow. The boundary values obtained by Eq. (21) are imposed across a single cell on the top boundary of the domain.

2.3.3. Outflow sponge layer

At the outflow boundary, a sponge region is added to reduce reflections from the outflow boundaries (Bodony, 2006). The damping parameters of the sponge region are adjusted through trial and error such that the reflectivity of sponge zones is minimized (Mani, 2010).

2.3.4. Kinematics conditions at the wall and the interface

No-slip boundary conditions are imposed for the rigid surface. At the interface, to ensure dynamic equilibrium, the traction force between the structure and flow has to be balanced,

$$\boldsymbol{\sigma}_s\cdot\mathbf{n}=\boldsymbol{\sigma}_f\cdot\mathbf{n} \tag{22}$$

where $\boldsymbol{\sigma}_f=-p\boldsymbol{I}+\boldsymbol{\tau}$ and for higher Reynolds numbers, the second term ($\boldsymbol{\tau}$) can be ignored. The kinematic boundary condition at the interface, to ensure no-slip condition, is expressed as $\boldsymbol{u}_f=\partial\boldsymbol{d}/\partial t$, where $\boldsymbol{u}$ and $\boldsymbol{d}$ are the velocity of the fluid and displacement of the solid at the interface, respectively.

2.3.5. Thermal conditions at the interface

For two-way thermally coupled simulations, the rigid wall is assumed to be isothermal at the recovery temperature. For the flexible part, the thermal condition has been satisfied at the interface of the panel and fluid by assuming zero net heat flux at the interface, which leads to $(\boldsymbol{q}_s+\boldsymbol{q}_f)\cdot\boldsymbol{n}=0$. Because of the no-slip condition, the wall temperature is the same for both the solid and fluid ($T_f=T_s$) at the interface. These boundary conditions at the interface are implemented by utilizing Eq. (A.6).

When the thermal solver is inactive, the isothermal condition is applied (including both rigid and flexible parts) at the interface with a specified temperature.

2.4. Initial conditions

Initially, flows over the rigid wall for each selected wall temperature were run till $tU/a=200$ when the flow develops and transient response passes. Compressible BL solutions described in Section 2.3.1 were used as the initial conditions for this stage of simulations. Once the flow reaches the desired state, the flow variables are saved and, later, these saved variables are used for continuing the simulations with the flexible panel for different Young's moduli such that all simulations have similar initial conditions. For the solid, the initial displacement, velocity, and acceleration of the panel are set to zero for all cases. For all cases with thermal interactions, the initial temperature of the panel is set as the recovery wall temperature.

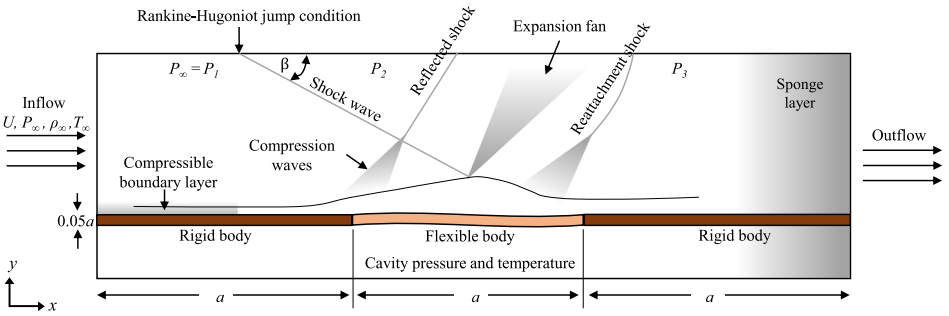

Fig. 3. Schematic of the computational domain, boundary conditions, simulation setup, and the main features of SBLI. The image is not to scale.

Table 1
The case number for base cases.

No.	Re_a	β	P_c/P_∞	κ_f	λ	M^*	κ_s	C_{p_s}	α_s
F1	39 000	35	1.0	–	61	0.02	–	–	–
F2	120 000	32.6	1.2	–	875	0.1	–	–	–
T1	120 000	32.6	1.2	5.5×10^{-5}	875	0.1	0.51	2.1	3.3×10^{-3}

2.5. Simulation setup and parameters

The computational domain is shown in Fig. 3 where the top partition (above the panel) is active and the bottom partition acts as a cavity with an inactive flow (not interacting with the panel). For all the simulations presented in the study, Mach number (Ma) is 2 and the inviscid shock impingement location is set at mid-panel, $x/a = 0$. The total length of the panel (including rigid and flexible parts) is $3a$, and the thickness of the panel is $0.05a$ (fixed for all cases). Here, the leading edge of the flexible panel starts at $x/a = -0.5$ and ends at $x/a = 0.5$. The Poisson ratio (ν_s) of the panel material is 0.45. For thermally coupled simulations, thermal conductivity ($\kappa_s T_\infty/\rho_\infty U^3 a$) of the panel is kept constant at 0.52.

Three base cases (F1, F2, and T1) have been selected in the present study with the parameters listed in Table 1. Parameters for Case T1 are used for all fully coupled thermal interactions. For the Case F1, the Reynolds number based on the panel length (Re_a) is fixed at 39000; boundary layer thickness at the inlet is $\delta/a = 0.02$, the shock angle (β) is 35° resulting in pressure ratio of $p_3/p_\infty = 1.8$. In this FSI system, the relative influence of fluid inertial forces versus solid elastic forces is characterized by a non-dimensional parameter known as non-dimensional dynamic pressure (λ). This parameter plays a crucial role in determining the stability of the coupled system. The non-dimensional dynamic pressure is defined as follows:

$$\lambda = \rho_\infty U^2 \frac{a^3}{D}, \quad D = \frac{Eh^3}{12(1-\nu_s^2)} \tag{23}$$

where D is referred to as bending stiffness or flexural rigidity, E is Young's modulus and ν_s is Poisson ratio. The non-dimensional dynamic pressure (λ) and mass ratio (M^*) used for different cases are listed in Tables 2 and 4.

Parameters of F2 and T-1 cases are chosen based on the Visbal (2014) and Li et al. (2019) where the panel oscillation with sustained limit cycle oscillations are observed. In these simulations, Reynolds number (Re_a) is fixed at 120000; boundary layer thickness at the inlet is $\delta/a = 0.01$, the shock angle (β) is 32.6° resulting in pressure ratio of $p_3/p_\infty = 1.4$. The mass ratio and dynamic pressure are $M^* = 0.1$ and $\lambda = 875$, respectively. These are the same parameters that are used for the verification of the FSI model. The solid structure for Case T1 is thermally active, hence we also report the non-dimensional thermal parameters e.g. specific heat ($C_{p_s} T_\infty/U^2$) and thermal expansion coefficient ($\alpha_\Delta T_\infty$) for this case.

2.5.1. Shock wave and boundary layer interaction over a rigid wall

In the first step, the shock boundary layer interaction over a rigid surface is explored with the primary aim to identify the specific range of wall temperature, shock angle, and Reynolds number that would exhibit the desired flow behavior for the subsequent simulations. Fig. 4(a) and (b) show the flow field for shock angles of $\beta = 32°$ and 35° at $Re_a = 39000$ for $T_w/T_r = 0.36$. At the shock angle of 32°, the pressure jump across the shock wave is not significant enough to generate a recirculation bubble. However, at $\beta = 35°$, the boundary layer is separated, and a recirculation bubble emerges. Simulation has also been conducted for $\beta = 38°$ (not shown here). Higher shock angles result in large pressure jumps, and a much larger domain size is needed to capture the dynamics in two-dimensional simulations. Here, considering the computational cost of the simulations, we limit our study to the shock angle of 35°. Fig. 4(c) presents simulation results for higher Reynolds number $Re_a = 80000$ for the same conditions as in Fig. 4(b). In this case, the laminar separation bubble becomes larger which is consistent with the findings in Visbal (2014), Katzer (1989). It is important to mention that in the laminar boundary layer, the length/size of the bubble is approximately one order larger than in the turbulent boundary layer (Robinet, 2007). In addition, a higher Reynolds number leads to a more intensified and energetic flow that shows wavy structures of the shear layers similar to Kelvin–Helmholtz's type instability. These wavy structures are responsible

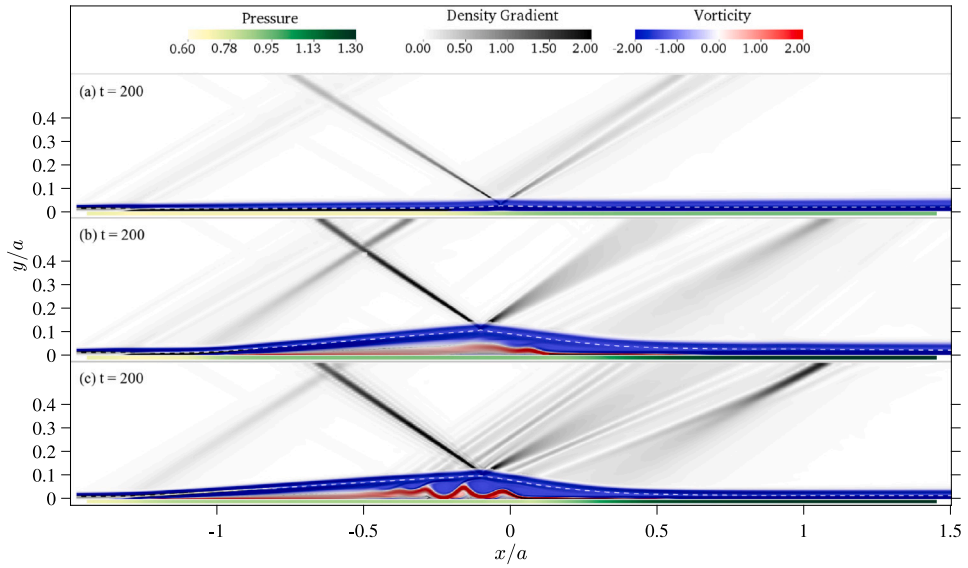

Fig. 4. SBLI over rigid surface at $T_w/T_r = 0.36$ for (a) $\beta = 32°$, (b) $\beta = 35°$ at $Re_a = 39000$, and (c) $\beta = 35°$ at $Re_a = 80000$.

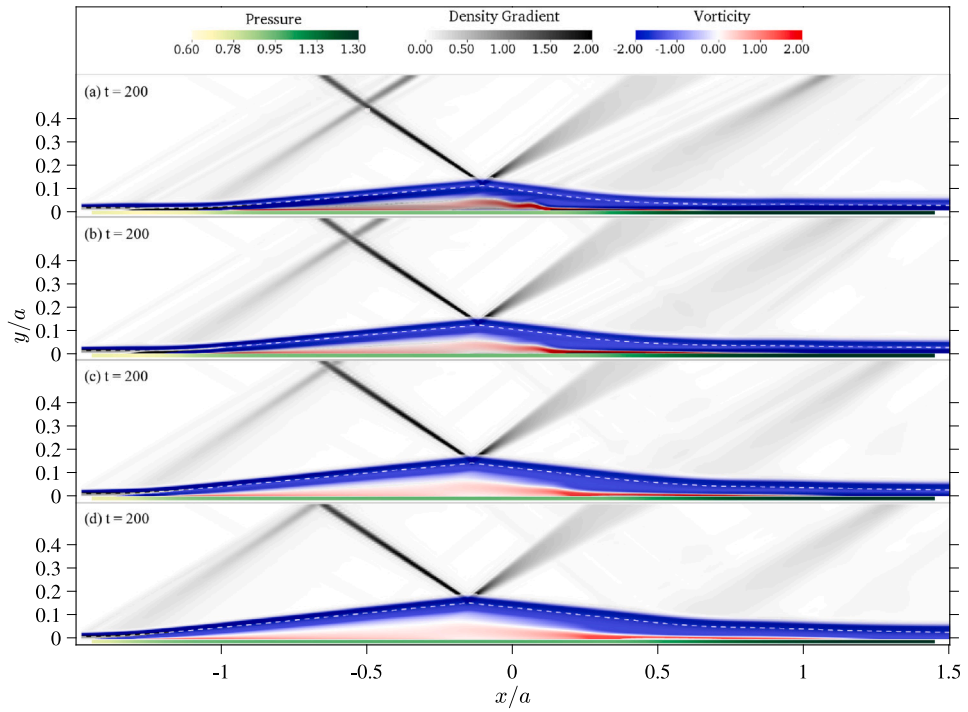

Fig. 5. SBLI over the rigid surface for $Re_a = 39000$ and $\beta = 35°$ at T_w/T_r = (a) 0.36, (b) 0.6, (c) 0.8 and (d) 1.0.

for the formation of several weaker shocks, along with the occurrence of separation and reattachment shocks. Based on the results obtained for the rigid surface, SBLI at $Re_a = 39000$ and $\beta = 35°$ is selected as a base scenario to test the role of panel flexibility and surface temperature in this study.

Fig. 5 compares the vorticity field of the boundary layers over a rigid surface for different thermal conditions (T_w/T_r = 0.36, 0.6, 0.8 and 1.0) at Re_a = 39000 and shock angle (β) of 35°. The flow field exhibits nearly all the essential characteristics of a typical SBLI, as depicted in Fig. 1. The primary difference is the expansion of the interaction region in the streamwise direction, which occurs as T_w increases. A decrease in wall temperature results in a reduction in the size of the separation bubble/interaction zone. This behavior aligns with the findings reported by Volpiani et al. (2018), where it is also emphasized that changes in the

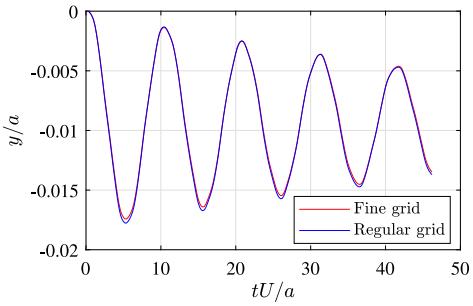

Fig. 6. Deflection at the middle of the compliant panel. The grid convergence test for the fine grid (1444 × 602) grid and the regular grid (722 × 301).

Table 2
Case numbers for studies referred in Section 3.1 (based on Case F1).

λ	T_w/T_r		
	0.36	0.6	0.8
61	C1T1	C1T2	C1T3
30	C2T1	C2T2	C2T3
6.1	C3T1	C3T2	C3T3

length of the interaction zone are primarily influenced by the incoming boundary layers. As the wall temperature increases, the fluid density decreases near the interface, leading to a decrease in momentum flux within the boundary layer. This reduction in momentum flux makes it easier for the boundary layer to separate, resulting in the formation of a larger separation bubble. Given the significant upstream influence associated with a wall temperature ratio of $T_w/T_r = 1.0$, requiring a more extended domain, our study is limited to the range of $T_w/T_r = 0.36 - 0.8$ for cases in Table 2. Despite the narrower range, this selection still enables us to accurately consider the variations in the length of the separation bubble and interaction zone resulting from changes in wall temperature.

2.5.2. Grid convergence study

The grid convergence study was performed to ensure grid-insensitive results as shown in Fig. 6. Here, two different fluid grid resolutions of 1444 × 602 and 722 × 301 are tested for $Re_a = 39000$, $\beta = 35°$, $P_c/P_\infty = 1$, $M^* = 0.02$ and $\lambda \approx 30$. Higher mesh resolution with mesh sizes of 0.033δ is supplied near the wall. The relative error for the mid-point panel displacement (shown in Fig. 6) is less than 2.0%. Based on the convergence study, the grid of 722 × 301 is used for the study of the FSI system, considering the computational cost and relative gain in the accuracy of the solution.

3. Results

3.1. Dynamically coupled FSI system

This section focuses on characterizing the transient behavior of SBLI over a flexible panel within a dynamically coupled FSI system where the system converges to an unexcited steady state. Parametric studies have been conducted to examine the influence of dynamic pressure, wall temperature, mass ratio, and cavity pressure while holding other parameters constant. To explore the impact of diverse conditions, we have taken into account various scenarios, as outlined in Table 2.

3.1.1. Effects of panel stiffness

The dynamics of shock wave and laminar boundary layer interactions are investigated for different levels of flexibility. In this subsection, we examine the effects of dynamic pressure at three specific values: $\lambda \approx 61$ (C1T1), 30 (C2T1), and 6.1 (C3T1)for a fixed wall temperature condition of $T_w/T_r = 0.36$.

The snapshots of the flow fields, when the plate is at its minimum and maximum deflected positions, are shown in Fig. 7 for $\lambda = 61$ case. At the maximum deflected position in Fig. 7(a), the negative slope of the panel's first half-length inhibits the formation of compression waves. Conversely, the reattachment shock intensifies due to stronger compression waves over the trailing half-length of the panel where the slope is positive. Also, the Kelvin–Helmholtz type instability structures in the recirculation zone lead to the formation of several weak shocks, parallel to the reattachment shock, between the expansion fan and reattachment shocks. The strength of this distributed shock structure is mainly influenced by the substantial deflection of the panel and its associated geometrical quasi-static influence on the low-frequency response of the recirculation bubble. In contrast, when the flexible panel returns to its minimum deflection state, as shown in Fig. 7(b), the separation and reattachment shock revert to their original states and the recirculation bubble resembles the flow observed over a rigid surface.

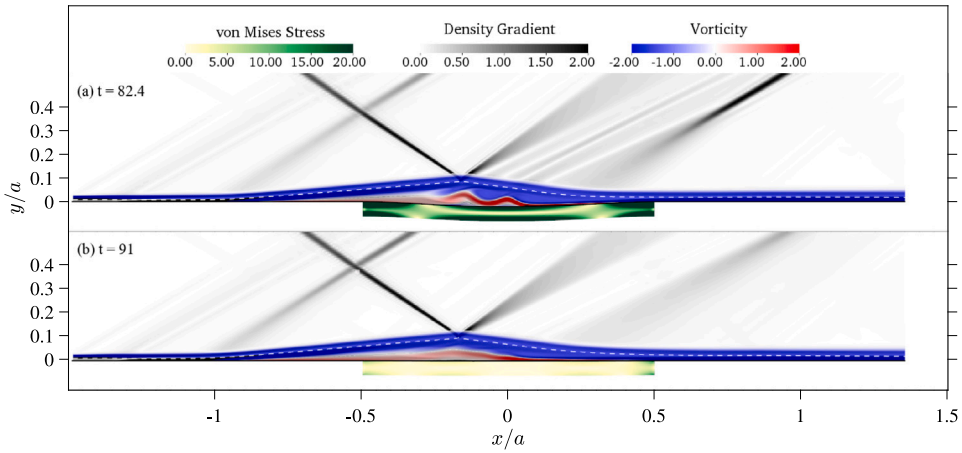

Fig. 7. SBLI over flexible panel at maximum and minimum deflection for C1T1.

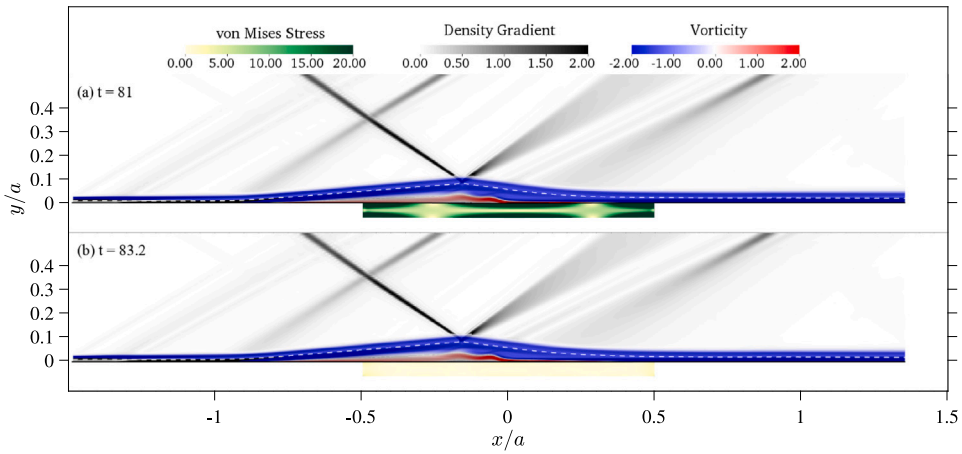

Fig. 8. SBLI over flexible panel at maximum and minimum deflection for C3T1.

Fig. 8 depicts snapshots of the flow fields for a panel with λ ten times smaller compared to the case illustrated in Fig. 7. The panel oscillates at different frequencies (three times faster than Case C1T1 as seen in Table 3) but with a smaller amplitude in Fig. 9. The flow fields exhibit almost similar characteristics at both maximum and minimum deflection. This is due to the smaller deflection amplitude in this case, which reduces the impact of geometrical changes. Essentially, the interface location remains relatively fixed, and the interaction between the flow and structure occurs through dynamic force and energy exchanges along the mean interface position. Unlike the Case C1T1, the length of the separation bubble, represented by the distance between the points in the separation and reattachment regions where the sign of skin friction changes, remains almost constant throughout the panel oscillation.

The conducted tests have revealed that the displacement number of the panel ($D_n = A/a$, where A is the amplitude) plays a crucial role in determining the SBLI response mode over flexible panels. It also dictates the relative significance of how the interface reconfiguration can modify the inherent flow dynamics compared to the dynamic interaction at the fluid–solid interface. For the weak FSI (panel deflection is significantly lower than the panel length), the mean separation size does not change (Varigonda and Narayanaswamy, 2023). Geometrical alterations of the interface have a more substantial impact on the boundary layer and shock structures than the dynamic interaction between the flow and structure and the reconfigurability of the elastic surface fundamentally governs the flow dynamics in this scenario. Shock-induced FSI differs from FSI without impinging shocks, where the primary driving factor for structural oscillation is the convective instability of the panel (Ostoich et al., 2013). In the case of a significant shock force on the panel, a notable deflection can occur, leading to geometric changes in the interface and quasi-static modification of the boundary layer.

In the aforementioned cases, SBLI induces panel oscillation with a diminishing amplitude over time, as illustrated in Fig. 9. The mid-point oscillation of the panel (similar to a damped sinusoidal) can be sufficiently represented as,

$$\Delta y(t) = Ae^{-\lambda_s t}\cos(\omega t + \phi) \tag{24}$$

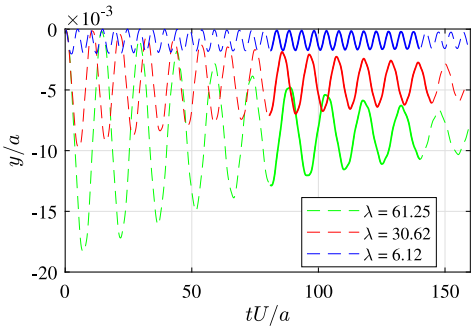

Fig. 9. The deflection at the shock impingement point for different λ. Solid lines enclose the period used for calculating average results.

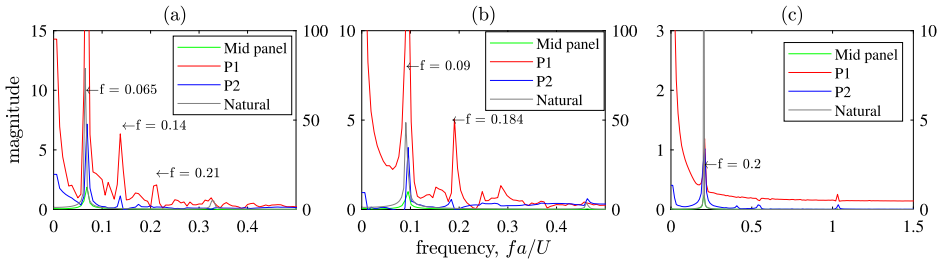

Fig. 10. Frequency-coupling between the modes of the panel deformation and the temporal oscillations associated with the separated shear layer for λ = (a) 61, (b) 30, and (c) 6.1 (probe P1: inside the bubble, probe P2: inside the expansion fan). Natural frequencies (black curve) are plotted on the right axis.

Table 3
Coefficients of damped sinusoid for different non-dimensional dynamic pressure.

	λ		
	61	30	6.1
Decay rate ($\lambda_s a/U$)	0.012	0.009	0.003
Frequency ($\omega a/U$)	0.068	0.093	0.203
Damping ratio (ζ)	0.168	0.091	0.014

where, A is the initial amplitude of oscillation, Δy is the displacement of shock impingement point around its mean deflected position, λ_s is the decay rate, ω is the angular frequency, and ϕ is the phase angle. The decay rate, frequency, and damping ratio ($\zeta = \lambda_s/\sqrt{\omega^2 + \lambda^2}$) obtained through curve fitting for cases C1T1, C2T1, and C3T1 are presented in Table 3. Due to the lower cavity pressure beneath the panel compared to the mean pressure on top of the panel, the panel primarily deflects downward in its first mode and oscillates around the mean deflected position. The panel vibrates at a higher frequency but with a lower amplitude when the λ is smaller or, equivalently when Young's modulus is higher (as depicted in Fig. 9).

The panel oscillation frequencies at the midpoint of the panel are analyzed for cases C1T1, C2T1, and C3T1, as depicted in Fig. 10. In the same figure, the natural frequencies of the structural system are represented by the black curves. The natural frequency is determined through structural simulations, where an impulse force of comparable magnitude to the fluid forces is applied to the center of the flexible panel for a duration of 5% of the natural oscillation period. In order to investigate the effects of coupling, two probes, namely P1 located within the separation bubble $(0, 0.015a)$, and P2 positioned within the expansion fan $(0.5a, 0.4a)$, are employed to monitor the temporal behavior of the flow. The responses of probes P1 and P2 are represented by red and blue curves, respectively. In Fig. 10(a), for Case C1T1, the peak at $fa/U = 0.065$ corresponds to the first mode of transverse motion of the panel. The natural frequencies of the structural system are slightly different from the corresponding values due to the presence of non-linear fluid actions in the coupled simulation. However, for all three cases (C1T1, C2T1, and C3T1), the first peak of probe P1 (red curve) coincides with the natural frequency (black curve) in the frequency domain. This alignment indicates that the flow within the bubble synchronizes with the oscillation frequency of the first mode of the panel, indicating a lock-in response behavior. In the case of C1T1 and C2T1, where the panel exhibits a lower frequency of oscillation but with larger amplitude, the first harmonic of the dominant mode of panel undulation is evident in probe P1 (red curves) at approximately $fa/U = 0.065$ in Fig. 10(a), and $fa/U = 0.09$ in Fig. 10(b). This observation indicates the presence of the first harmonic due to the surface reconfiguration. However, at higher frequencies and smaller amplitudes, the harmonic is not observed due to the damping characteristics of the fluid, as well as the diminished amplitude and smaller timescale of the oscillation. As for probe P2 in the expansion fan region, the weaker waves are damped out, thus the harmonics are not observed.

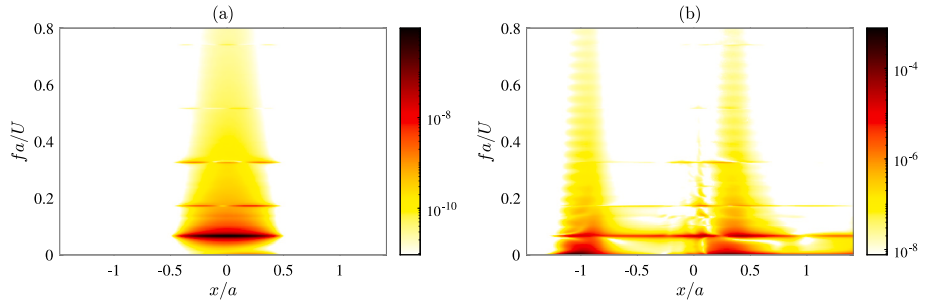

Fig. 11. PSD of (a) panel deflection and (b) surface pressure for Case - C1T1.

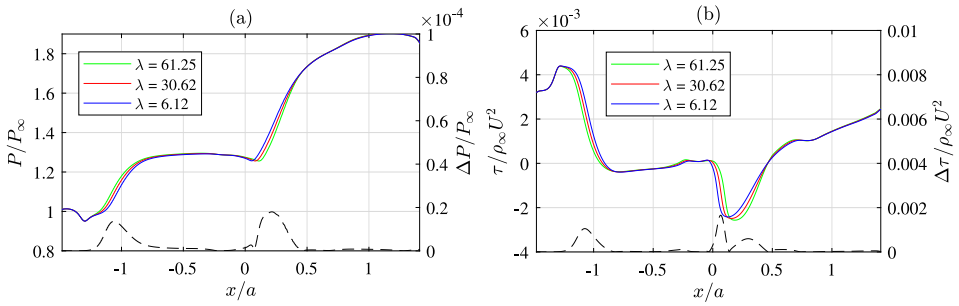

Fig. 12. (a) Pressure profile and (b) shear stress on the surface of the panel for cases C1T1, C2T1, and C3T1. The dashed line shown on the right y-scale depicts the absolute difference between Case C1T1 and C3T1.

Fig. 11 illustrates the changes in frequency along the x-axis where three mode shapes can be clearly identified in Fig. 11(a) along with a broadband frequency. The corresponding footprint of these oscillations can be seen in the pressure PSD shown in Fig. 11(b) in addition to the very low-frequency oscillations. The upstream and downstream influence of panel oscillation on the surface pressure is reflected in Fig. 11(b) at $fa/U = 0.067$.

Fig. 12 illustrates the time-averaged surface pressure and shear stress on the panel for cases C1T1, C2T1, and C3T1. The time averaging window is highlighted with a solid line in Fig. 9. Throughout the paper, the time-averaging window contains at least 4 mid-panel oscillations and is conducted once the transient state is passed. For the simulation with decaying oscillation, the time window is selected from the end of the simulation so that the averaging results are close to the steady-state condition. In Case C1T1, where the panel oscillates with a higher amplitude, a slight increase in the length of the separation bubble is observed. Despite the influence of λ on the instantaneous flow field (as depicted in Figs. 7 and 8), the average pressure on the panel's surface remains similar except in narrow regions with significant pressure gradients.

Over time, the flow field of the underdamped FSI system reaches a pseudo-steady state. In Case C1T1, for instance, it takes approximately $tU/a = 500$ to attain this state. The pseudo-steady state is defined as the point where the amplitude of panel oscillation becomes less than 1/30th of the boundary layer thickness, and the panel's response to the flow becomes negligible. The final deflection of the panel in this pseudo-steady state is primarily a function of Young's modulus and cavity pressure.

3.1.2. Effects of mass ratio

The dynamics of the interaction were studied for three different mass ratios ($M^* = 0.02, 0.04$, and 0.2) at a fixed $\lambda = 61$. The mid-panel deflection is shown in Fig. 13(a) and the system's behaviors are summarized in Table 4. The panel's motion almost follows the empirical relation $\omega_n = \sqrt{k/m}$, analogous to a classical mass–spring–damper system. As expected, the results indicate that the oscillation frequency increases with decreasing panel density or increasing mass ratio. Additionally, there is a strong correlation between the panel's density and the decay rate of vibration. Reducing the panel's density leads to a higher decay rate. In this model, the damping of the system solely arises from the fluid, as the internal damping of the panel material is not considered. Consequently, if the panel's mass is low, the fluid can dampen the panel's motion more rapidly. Notably, for all different mass ratios, the displacement at the midpoint converges to the same unexcited position in Fig. 13(a). This is because the final deformed and steady state of the panel depends only on its stiffness and the pressure difference across it.

3.1.3. Effects of cavity pressure

The cavity pressure is another parameter that can significantly influence the interaction. It plays a crucial role in determining the mean or final steady-unexcited state deflection profile of the panel. To examine the effects of cavity pressure on panel oscillation,

Table 4
Coefficients of damped sinusoid for different mass ratio.

	Mass ratio, (M^*)		
	0.02	0.04	0.2
Decay rate ($\lambda_s a/U$)	0.013	0.017	0.029
Frequency ($\omega a/U$)	0.068	0.097	0.211
Damping ratio (ζ)	0.189	0.170	0.135

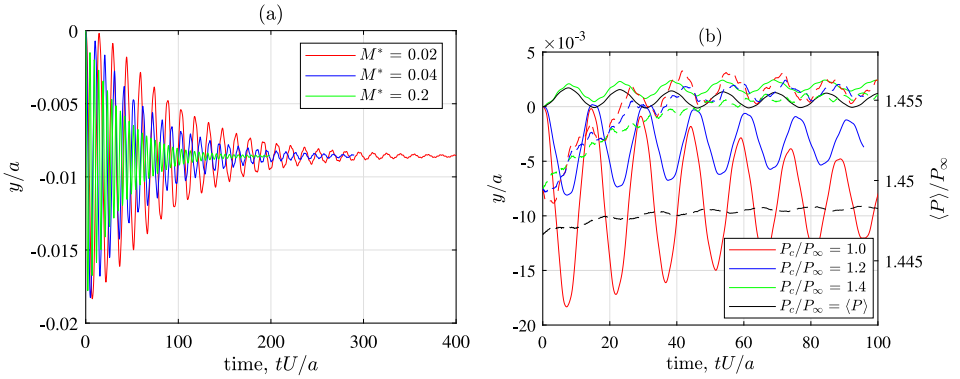

Fig. 13. (a) Deflection at the shock impingement point for different mass ratios. (b) The deflection at the shock impingement point for different cavity pressures of $P_c/P_\infty = 1.0$, 1.2, 1.4 and $\langle P \rangle$, where $\langle P \rangle$ is the spatial average pressure on the top panel surface at the time t.

we cross-compare $P_c/P_\infty = 1.0, 1.2, 1.4$, and the case with spatial average surface pressure on the top of the panel $\langle P \rangle$ defined as,

$$\langle P(t) \rangle = \frac{1}{L} \int_0^L P(x,t) dx. \tag{25}$$

As shown in Fig. 13(b), the midpoint of the panel exhibits different behaviors depending on the cavity pressure. The mid-point of the panel oscillates below its initial state for $P_c/P_\infty = 1.2$ and the opposite behavior is observed for $P_c/P_\infty = 1.4$ where the amplitude is always position positive. The mid-point of the panel oscillates around the mean position with a lower amplitude for the case where the cavity pressure is equal to the spatial average pressure. The mean deflection of the mid-point will be positive for this condition since the endpoint of the pressure plateau is slightly shifted downstream of the shock impingement point determining the final pseudo-steady state of the panel's deflection. In experiments, the panel usually buckles to a concave/convex shape (locked in its first-mode shape) if the panel thickness is very small (lower mechanical impedance) (Vasconcelos et al., 2023; Daub et al., 2022). Additionally, for a time-invariant cavity pressure, the frequency exhibits a slight decrease as the magnitude of the cavity pressure increases. The changes in spatially averaged surface pressure between different cases are very small as seen on the right axis in Fig. 13(b). We have observed a phase difference of 90° between the pressure and the deflection. Interestingly, for the case with variable cavity pressure, the average pressure of the top surface is slightly lower than in other cases.

3.1.4. Effect of side wall kinematic boundary conditions

To examine the role of side wall kinematic boundary conditions on the dynamics of the panel, the simply-supported and clamped end conditions were investigated for Case F2 in Table 1. These specific conditions were chosen as they are known to exhibit limit-cycle oscillations in the system (Li et al., 2019; Visbal, 2014). Fig. 14 presents a comparison between the fixed–fixed and pinned–pinned boundary conditions for the panel. The fixed–fixed configuration exhibits low amplitude and high-frequency oscillations, characterized by a rapid decay rate. Conversely, the pinned–pinned condition showcases more sustained panel oscillations with larger amplitude, slightly lower frequency, and a relatively slower decay rate. Although the simulation parameters are consistent with the validation case and the findings in Li et al. (2019), where a limit cycle oscillation was observed, the oscillation behavior in this study resembles damped sinusoidal motion. This behavior can be attributed to the well-known Timoshenko effect, which encompasses shear deformation and rotational bending effects, including the nonlinear effects arising from the thickness of the beam. The dominant frequency observed for the fixed–fixed and simply-supported conditions is 0.053 and 0.037, respectively. In the case of the fixed–fixed panel, the additional resistance at both ends increases the damping effects leading to a higher decay rate of the oscillation. However, it should be noted that although the simply supported condition exhibits more dynamic behavior, panels with such boundary conditions have lower structural integrity and safety factors. Consequently, these types of panels are rarely utilized in practical applications. Therefore, this study primarily investigates the fixed–fixed boundary conditions, which are more commonly encountered and have better practical applicability.

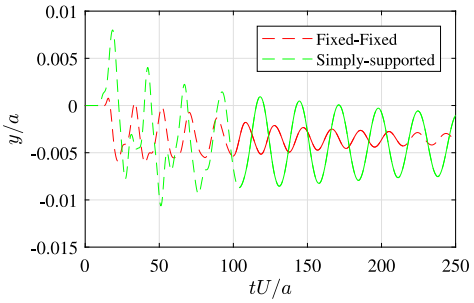

Fig. 14. Mid-panel oscillations for simply supported and clamped beams.

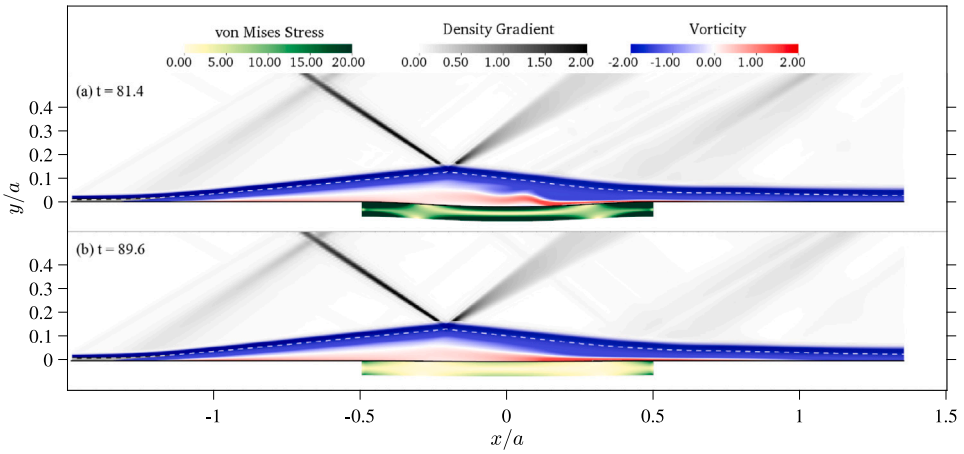

Fig. 15. SBLI over flexible panel at maximum and minimum deflection positions for Case C1T3. Grayscale: density gradient; Blue to red: vorticity inside the boundary layer and interaction zone; and Yellow to green: von Mises stress.

3.1.5. Effects of wall temperature (in the absence of coupled-thermoelastic forces in the panel)

This section aims to investigate the combined effects of wall cooling and panel flexibility, considering thermally independent structural properties. Simulations were conducted with fixed wall temperatures below the recovery temperature, specifically at $T_w/T_r = 0.36$, 0.60, and 0.80. If the wall temperature is equivalent to the recovery temperature, the wall behaves similarly to an adiabatic wall. If the wall temperature exceeds T_r, it induces a heating effect, while a cooling effect happens for t lower wall temperatures. In the case of cold wall conditions, the most noticeable observation is the reduction in the thickness of the incoming boundary layer and the interaction region. When the wall is cooled, the fluid density within the boundary layer increases, resulting in a higher rate of momentum transfer from the outer layer to the inner layer. As a result, the separation of the boundary layer is impeded, leading to slower growth of the boundary layer and a smaller interaction region. For example, in the case of C1T1 shown in Fig. 7, the thickness of the interaction zone (i.e., the vertical distance from the panel to the Mach line with $Ma = 1.0$) is measured to be $0.19a$ at $x/a = -0.5$, which is where the flexible panel begins. In contrast, for C1T3 depicted in Fig. 15, the thickness of the interaction zone at the same location is observed to be $0.15a$.

By comparing the flow fields of cases C1T1 and C1T3 depicted in Figs. 7 and 15, respectively, several observations can be made. In the case with a lower wall temperature (C1T1), the shear layer within the interaction region exhibits a steeper gradient compared to the case with a higher wall temperature (C1T3). This non-linearity arises from the combined effects of the panel motion and the reverse flow, resulting in a wavy shear layer reminiscent of Kelvin–Helmholtz instability. Furthermore, unlike in Case C1T1, the strength of the separation and reattachment shocks remains similar at both the maximum and minimum deflection positions in Case C1T3, as shown in Fig. 15(a) and (b). This suggests that the higher wall temperature in C1T3 leads to a wider extent of the interaction region. As a result, compression waves may emerge over a larger spatial range, contributing to the observed behavior.

Quite different from what has been seen for panel stiffness or density, the influence of wall temperature on the timescale of oscillation is relatively small, as demonstrated in Fig. 16. Even though the panels with different temperatures initially oscillate at the same amplitude, over time, the cumulative effect of different temperature conditions slowly causes their oscillation amplitudes to deviate from one another. All these panel oscillations were fitted into the Eq. (24) and the coefficients are depicted in Table 5.

The frequency of panel oscillation remains relatively constant across all wall temperatures for different values of λ. However, other oscillation parameters, such as the decay rate or damping ratio, change with the wall temperature. In Table 5, it can be observed that the decay rate decreases as the wall temperature increases in cases with higher λ values. This can be attributed to

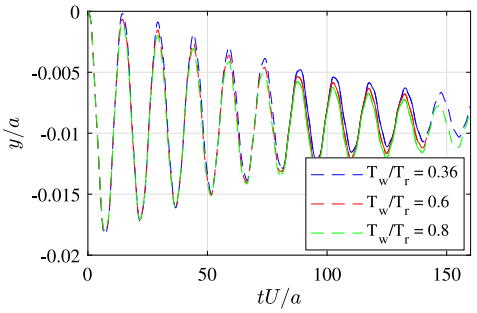

Fig. 16. The deflection at the shock impingement location for different wall temperatures. The solid line encloses the period used for the calculation of the average results.

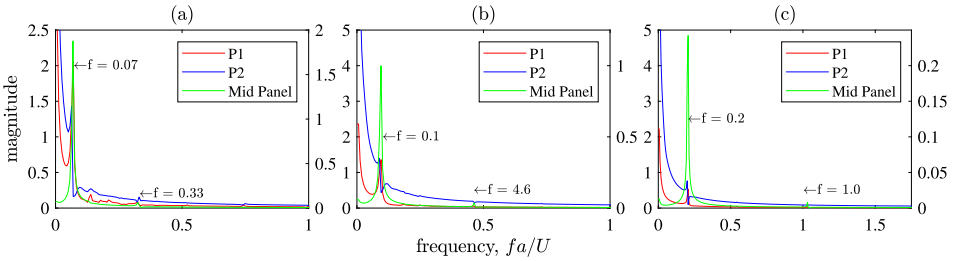

Fig. 17. Frequency-coupling between the modes of the panel deformation and the temporal oscillations associated with the separated shear layer for cases (1) C1T3, (b) C2T3 and (c) C3T3, Probe P1: inside the bubble, Probe P2: inside the expansion fan. The left y-axis is for the green curve and the right axis is for the red and blue curves.

Table 5
Coefficients of the damped sinusoid for all the cases listed in Table 2.

	Amplitude, A/a			Decay rate, $\lambda_s a/U$			Frequency, $\omega a/U$			Damping ratio, ζ		
	T1	T2	T3	T1	T2	T3	T1	T2	T3	T1	T2	T3
C1	0.01	0.009	0.009	0.012	0.011	0.011	0.068	0.068	0.068	0.168	0.162	0.161
C2	0.005	0.005	0.005	0.008	0.009	0.008	0.093	0.093	0.093	0.09	0.091	0.085
C3	0.001	0.001	0.001	0.003	0.003	0.003	0.203	0.204	0.204	0.014	0.013	0.015

the stronger separation bubble at lower wall temperatures, causing the panel to lose more energy per oscillation cycle. Conversely, at higher wall temperatures, the separation bubble is influenced more by the geometric effect of panel deflection, resulting in the panel losing less energy per cycle. On the other hand, for cases with small values of λ, higher wall temperatures lead to a larger decay rate. This is particularly noticeable when the oscillation frequency is very high. In these cases, the FSI coupling weakens, and since the panel experiences a more uniform pressure profile at higher wall temperatures, its energy loss rate is lower. Overall, while the frequency remains nearly constant, the decay rate and damping ratio of the panel oscillation are influenced by the wall temperature, highlighting the complex interplay between FSI and thermal effects.

In the cases of C1T3, C2T3, and C3T3 with a wall temperature of $T_w/T_r = 0.8$, as depicted in Fig. 17, the probe P1 positioned inside the separation bubble does not exhibit any harmonics, unlike what was observed in the cases with $T_w/T_r = 0.36$ (Fig. 10). Instead, these cases only show the first mode of the oscillation for all dynamic pressure. The higher wall temperature significantly alters the dynamics of the interaction within the bubble.

Figs. 18(a) and (b) present the average pressure and shear stress on the panel for different wall temperatures. The pressure distribution along the wall exhibits a two-step increase, as depicted in Fig. 18(a). In the flat region of the pressure plateau, ranging from $x/a = -0.75$ to $x/a = 0.025$, the wall shear stress remains similar for all wall temperatures. It is found that for minimum wall temperature (Case C1T1), the length of the separation region is approximately $1.5a$ whereas, for maximum wall temperature (Case C1T3), the length increases to $2.2a$ (almost 1.5 times larger). Higher wall temperatures result in larger separation bubbles. Within the recirculation bubble region, the pressure and shear stress remain mostly constant and uniform from $x/a = -0.75$ to $x/a = 0$ (the location of shock impingement). This occurs because the reverse flow within the separation bubble is driven by the adverse pressure gradient, which is influenced by the strength of the shock wave. Since the shock angle remains constant, the velocity of the reverse flow in that specific zone remains the same, resulting in comparable shear stress values. At $x/a = -0.25$ to 0, the shear stress crosses the zero line, indicating the formation of another reverse flow, referred to as a secondary bubble, which is consistent with observations in Robinet (2007). The rapid drop in the shear stress after $x/a = 0$, suggests the occurrence of faster reverse flow.

The spatial distribution of the average surface pressure difference between the highest and lowest λ is depicted in Fig. 19 for all tested wall temperatures. Near $x/a = 0.15$, which corresponds to the base of the reattachment shock, the largest disparity in

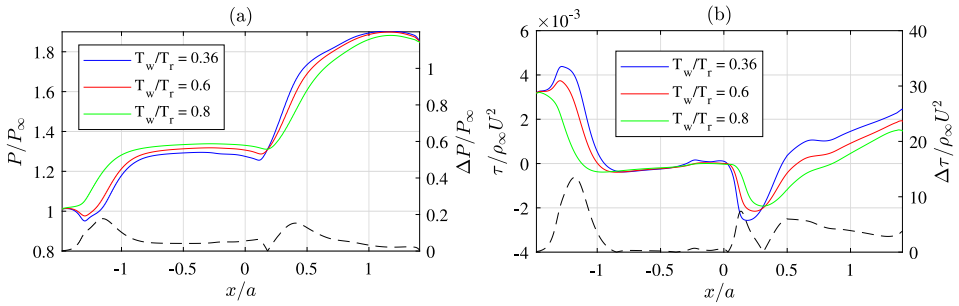

Fig. 18. The effect of wall temperatures on the average (a) surface pressure and (b) shear stress for Case C1T1, C1T2, and C1T3. The right axis (dashed lines) shows the absolute value of the difference between Case C1T1 and Case C1T3.

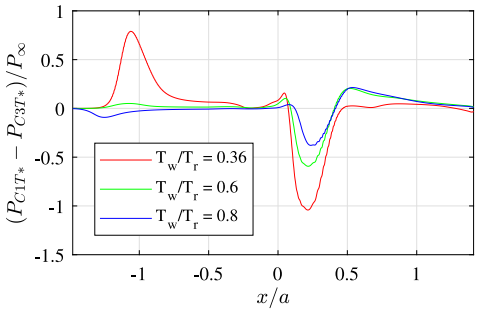

Fig. 19. Difference between the average wall surface pressure for the case with maximum (C1T∗) and minimum (C3T∗) non-dimensional dynamic pressure. In the y-axis label, the terms P_{C1T1} and P_{C3T1} are the surface pressure for the cases with $\lambda = 61$ and $\lambda = 6.1$, respectively, at $T_w/T_r = 0.36$ (red curve). (For interpretation of the references to color in this figure legend, the reader is referred to the web version of this article.)

wall pressure is observed for the lowest wall temperature case. This aligns with the region exhibiting the highest surface pressure gradient. The higher curvature of the panel at this specific location causes the flow to undergo a more substantial pressure gradient, resulting in greater pressure variations along the panel. These findings suggest that the impact of surface flexibility is more noticeable in cold wall cases compared to scenarios with higher wall temperatures.

3.2. SBLI behavior of thermally coupled FSI system

To gain a deeper understanding of the significance of fully coupled thermal interactions, we conduct a comparative analysis between the deflection of the panel in two scenarios: one involving an adiabatic condition (FSI of Case F2 in Table 1) and the other with thermal coupling (FTSI of Case T1). This analysis considers both fixed–fixed and simply supported sidewall boundary conditions. Fig. 20(a) shows that during the transient phase, both cases exhibit a similar deflection profile. However, as time progresses, a slight deviation of the panel deformation has been observed between the thermally coupled system and the adiabatic system. Since only the top surface of the panel interacts with the flow and the other three surfaces are kept adiabatic, the panel acts as a medium of slow heat conduction from the leading part of the panel to the trailing part as illustrated in Fig. 21. Above the transient phase at $tU/a = 150$, the blue region illustrates heat absorption into the panel and the red region shows the heat supplied into the flow. Another discussion on the comparison of the FTSI system is available in Appendix C, which illustrates a comparison between the surface pressure of this thermally coupled case and the predicted surface pressure based on local piston theory. The observed response mode is found to be reasonably estimated using the piston-theory unsteady force.

Moreover, for the simply supported sidewall boundary conditions, the deflection in the coupled simulation deviates more significantly from the adiabatic cases compared to the fixed–fixed sidewall boundary conditions. This is attributed to the higher amplitude of the panel deflections, which allows for a more pronounced thermal interaction within the system.

3.2.1. Effects of thermal expansion coefficient and specific heat

Subsequent simulations were performed for different specific heat and thermal expansion coefficients, as listed in Table 6, while keeping the remaining parameters from Case T1 in Table 1 constant. The spatially averaged wall temperature and Nusselt number (a non-dimensional measure of heat flux) are plotted in Fig. 22.

As anticipated, higher specific heat (i.e. increased heat absorption and storage capacity) results in a nearly constant panel temperature over the whole simulation duration ($tU/a = 3000$). Conversely, for lower specific heat values (such as in cases T-12a and T-22a), a gradual decrease in surface temperature is observed. Here, the initial temperature of the panel is close to the theoretical recovery temperature ($T_r/T_\infty = 1.678$), while the fluid temperature adjacent to the wall is slightly lower ($T/T_\infty = 1.669$) than the

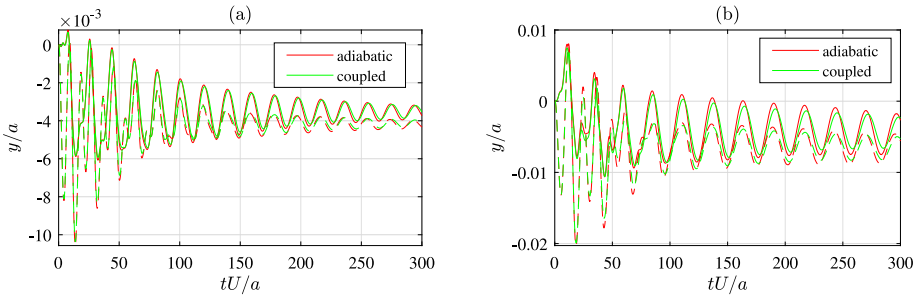

Fig. 20. Mid-panel deflection (solid line) and 3/4th chord length deflection (dashed line) for adiabatic and thermally-coupled simulation with (a) fixed–fixed and (b) simply supported sidewall boundary conditions.

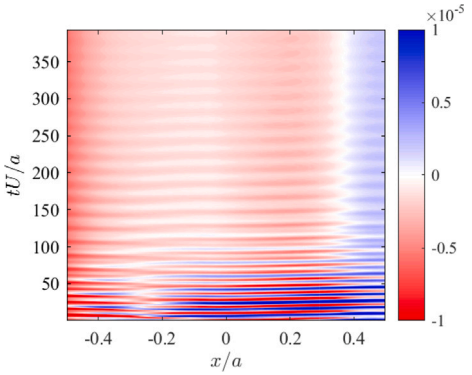

Fig. 21. Space–time plot of the nondimensional heat flux for Case T1.

Table 6
Case numbers for the thermally coupled system (based on Case T1 mentioned in Table 1) with non-dimensional parameters.

No.	α_s	C_{p_s}	T_{bw}/T_∞
T-11a	3.3×10^{-3}	2.1	adiabatic
T-12a	3.3×10^{-3}	2.1×10^{-3}	
T-21a	6.6×10^{-5}	2.1	
T-22a	6.6×10^{-5}	2.1×10^{-3}	
T-11c	3.3×10^{-3}	2.1	1.0
T-12c	3.3×10^{-3}	2.1×10^{-3}	
T-22c	6.6×10^{-5}	2.1×10^{-3}	
T-11h	3.3×10^{-5}	2.1	2.0

theoretical recovery temperature. During the initial transient phase of the simulations (from $tU/a = 0$ to 75), the Nusselt number exhibits similar behavior for different specific heat and thermal expansion coefficients. However, after this initial phase, deviations in panel motion among cases with different specific heat values become apparent. Since the stress-free temperature corresponds to the recovery temperature, and the panel temperature remains close to the recovery temperature, the thermal expansion coefficient does not noticeably affect the panel's oscillations or thermal interaction behavior. At this stage, the panel demonstrates a thermally weak coupling behavior.

3.2.2. Effects of cooling through the bottom wall

To introduce a cooling effect in the interactions, the temperature of the bottom wall of the panel is lowered to the freestream temperature T_∞, while the temperature of the side walls is maintained at a constant value of T_r.

The x–t plot of panel deflection is shown in Fig. 23 and 3/4th chord length deflection is shown in Fig. 25(a) for cases T-11a, T-11c, T-12c, and T-22c. The panel response is shown on the frequency domain in Fig. 25(b). Spatially averaged temperature over the top wall is shown in Fig. 25(c) for the same cases For reference, the result for an adiabatic wall (Case T-11a) is also included. An inset plot is also provided in Fig. 25(c) to illustrate the small changes in temperature for different cases when the difference is small. Here, the y-axis is shifted to $(\langle T\rangle/T_\infty) - 1.05$ for better representation.

In Case T-11c, which has a moderately higher specific heat, the wall temperature gradually decreases over the time span of $tU/a = 0$ to 100, following an exponential decay curve, until it reaches a constant value of $1.05T/T_\infty$. As expected, for the lower

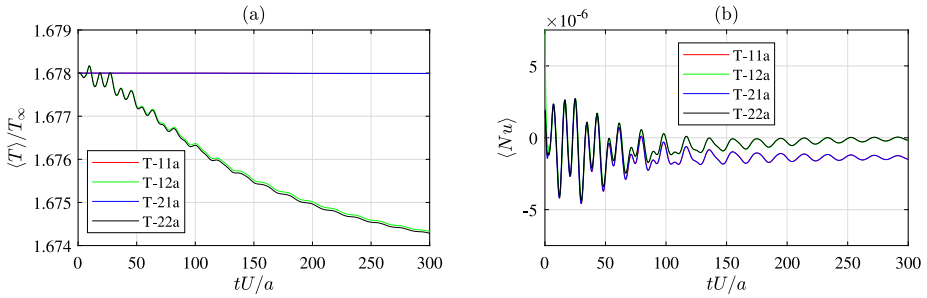

Fig. 22. Spatially averaged (a) wall temperature and (b) Nusselt number on the top surface of the panel.

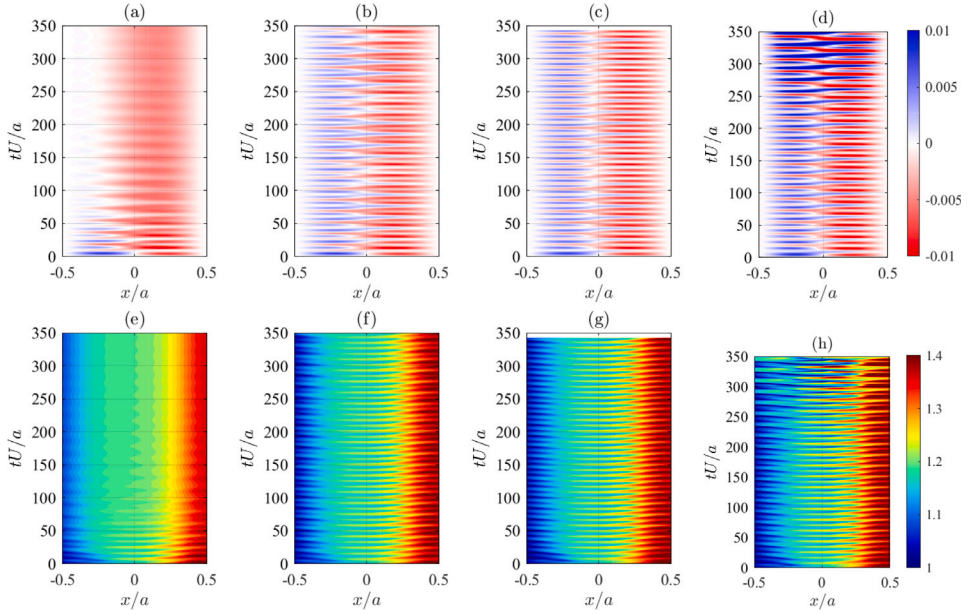

Fig. 23. *x–t* plot of panel deflection (top row) and pressure (bottom row) for Case (a) T-11a (b) T-11c (c) T-12c, and (d) T-22c.

specific heat values in cases T-12c and T-22c, the temperature on the top surface experiences a sudden drop as the bottom wall is maintained at a cold temperature with a continuous heat supply into the system.

Notably, the cases T-11c and T-12c exhibit sustained panel oscillations even with fixed–fixed sidewall boundary conditions, as illustrated in Fig. 23(b), (c) and Fig. 25(a), in contrast to the adiabatic case. Notably, the panel motion in these cases consists of multiple frequencies. For Case T-11c, the panel oscillates within a fixed range of amplitude. On the other hand, Case T-22c demonstrates a gradual increase in the amplitude of panel oscillations when compared to the adiabatic case.The frequency domain shows the first peaks at $fa/U \approx 0.051, 0.056, 0.055, 0.055$ and the second peaks at $0.11, 0.12, 0.12, 0.11$ for the cases of T-11a, T-11c, T-12c, and T-22c, respectively in Fig. 25(b). The former frequencies pertain to the first mode shape of oscillation, while the latter corresponds to the second mode shape, as evidenced by Fig. 24(a). In the initial three cases exhibiting damped/sustained oscillations, the second peaks do not align perfectly as harmonics (i.e., they are not exact integer multiples of the first frequency). Another interesting finding is that for Case T-22c, the deflection experiences a gradual increase. Eventually, it stabilizes into a limit cycle oscillation with a notably higher amplitude after a prolonged duration. For this case, the second frequency is a perfect harmonic of the first mode. On the time–frequency domain in Fig. 26(a), the second mode of oscillation dies very quickly after the panel starts to oscillate for the adiabatic Case T-11a. However, for the thermally coupled cases, both modes of oscillation were sustained during the whole simulation time.

The frequency of the surface deflection, pressure, temperature, and heat flux is shown in Fig. 24 both the first and second modes of panel oscillation become dominant. The impact of these oscillations is reflected in the other surface properties (pressure, skin friction, and heat flux) downstream of the panel till the end of the domain. However, the upstream impact of the oscillation is very small. Inspecting Fig. 24(d), it is observed that the dynamic behavior of the thermal interaction is mainly reflected near the ends of the panel. For the turbulent boundary layer, the impact of the panel motion on the surface properties downstream of the separation zone diminishes within a distance of $3\delta_{99}$ (Spottswood et al., 2019). However, in this laminar boundary layer study, this distance is more than $50\delta_{99}$.

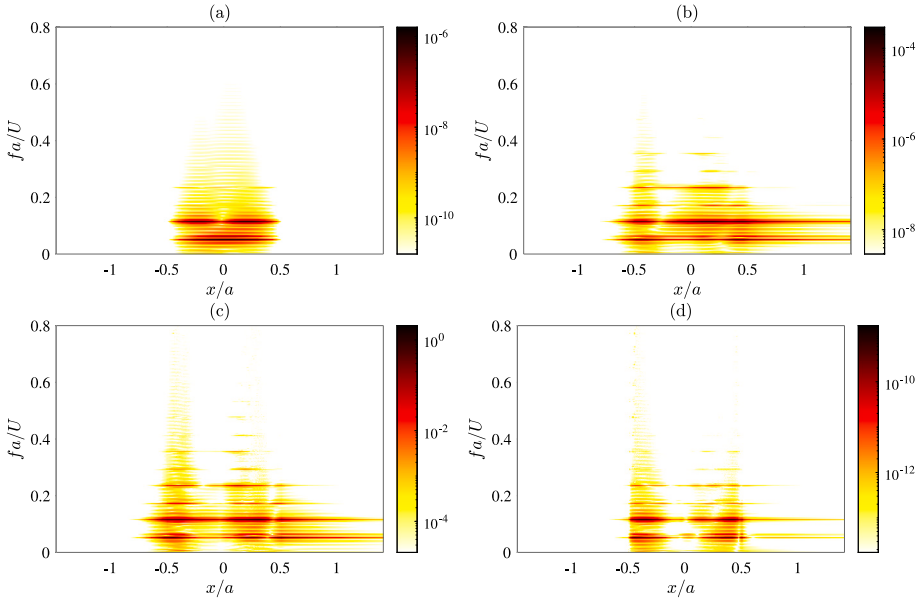

Fig. 24. PSD of (a) panel deflection, (b) surface pressure, (c) temperature, and (d) heat flux for Case T-11c.

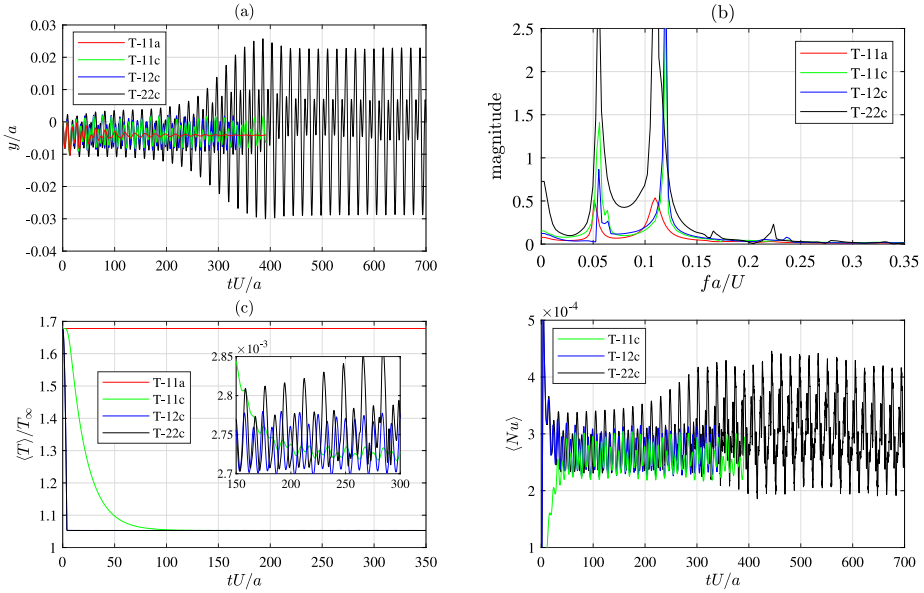

Fig. 25. (a) 3/4th chord length deflection, (b) frequencies of the 3/4th chord length deflection, (c) spatially averaged top-wall temperature (inset showing small changes), and (d) spatially averaged non-dimensional heat-flux for the cases with heat extracted through the bottom surface of the panel.

A colder wall increases the density of the adjacent fluid which in turn increases the average momentum flux into the boundary layer (Volpiani et al., 2018). Volpiani et al. also observed that wall cooling increases the root-mean-square wall pressure i.e. the dynamic loads for turbulent flow even though the separation zone decreases (Volpiani et al., 2018). Similarly, for Case T-11c, once the panel experiences this increased momentum flux and dynamic load, it oscillates at a sustained frequency and thus shows a limit-cycle oscillation, unlike the adiabatic cases. In the case of T-12c, the lower specific heat enables a rapid temporal change in temperature within the panel, as indicated by the inset image in Fig. 25(c). Hence, Case T-12c exhibits a stronger thermal coupling with the flow, akin to the canonical scenario of a cold isothermal wall. The heat flux depicted in Fig. 25(d) exhibits a pronounced correlation with the amplitude of panel oscillation. This strengthened heat transfer mechanism facilitates a greater transfer of momentum from the fluid to the panel, resulting in a gradual increase in the panel's amplitude over time.

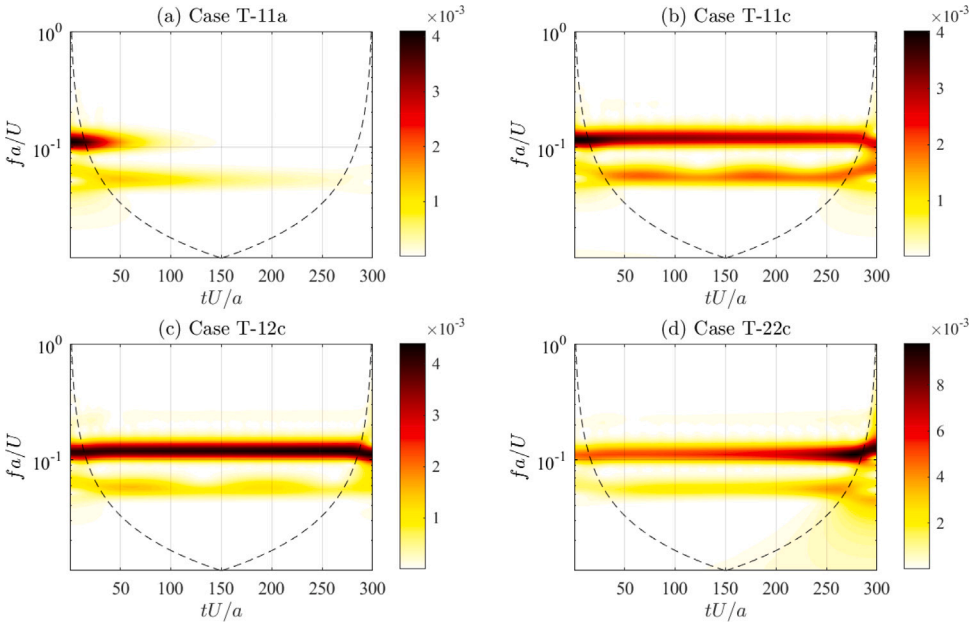

Fig. 26. Panel deflection response at 3/4th chord length on time–frequency domain for (a) T-11a, (b) T-11c, (c) T-12c, and (d) T-22c. The black dashed line shows the cone of influence of the boundary.

The oscillation pattern of the panel suggests that there is a simultaneous mode switch between the first and second modes of the panel's oscillations during one cycle of the oscillation in Fig. 27(a) and (g). A similar mode switch is also observed for the laminar SBLI with smaller amplitude of the second mode deflection profile (Li et al., 2019). For a turbulent boundary layer study, Spottswood et al. observed an intermittent transition between the large amplitude first mode shape to the small amplitude second mode shape (Spottswood et al., 2019). To elucidate the dynamic behavior of the panel deformation and the underlying flow physics, the time period of one cycle is divided into four distinct intervals, as depicted in the x–t plot of Fig. 27:

- Phase-1: During this phase, the deflection at the mid-point and 3/4th chord length are out-of-phase, and the mid-point of the panel is moving upward.
- Phase-2: In this phase, the mid-point and the point at 3/4th chord length remain in-phase and continue moving upward.
- Phase-3: In this phase, both points are in-phase while the panel itself is moving downward.
- Phase-4: This phase marks the points becoming out-of-phase again, with only the mid-point moving downward.

It is noted that the line colors (vary with time) in Fig. 27(f) correspond to the colors of the curves in sub-figures (g–k). During phase-1, the fore part of the panel experiences a lower pressure compared to the average, whereas in the second half, the pressure becomes relatively higher. This pressure differential between the two halves of the panel induces an upward motion in the first half and a corresponding downward motion in the second half, resulting in the observed deformation pattern where the motion at the mid-point and 3/4th chord length are out-of-phase.

Towards the end of phase-1, a portion of the fore part of the panel moves into the fluid, pushing the boundary layer upward and creating a lower pressure region on the panel between $x/a = -0.2$ to 0.2. At this stage, the aft part of the panel reaches its maximum deflection, and hence a large potential elastic energy is stored in the aft part of the beam. The accumulation of significant restoring elastic energy, coupled with the pressure decrease in the second part of the panel, drives the aft portion upward. On the fore part, even though the pressure difference is positive at the beginning of phase-2, the panel slightly moves downward direction due to the positive momentum in the fore part of the panel, as can be seen in Fig. 27(h).

At the onset of phase-3, we have a significant pressure difference on the fore part of the panel ($x/a = -0.5$ to 0.3). Meanwhile, the momentum of the panel in the second half lowers, as evidenced by the nearly negligible v-velocity depicted in Fig. 27(h). In the second half of the panel, due to higher pressure force and release of stored elastic potential energy, especially between $x/a = -0.1$ and 0.4, the aft part of the panel moves downward direction. At the end of this phase, the panel deflection completely resembles the second-mode shape.

At the beginning of phase-4, the momentum of the panel concentrates around the center ($x/a = -0.25$ to 0.25) of the panel. Compared with other stages, the pressure difference is the smallest (spatial average of the pressure difference from the start to end of the panel) at this stage. Neither the pressure difference nor the momentum drives the motion of the panel. However, in this position, the panel is at its maximum deformed state (the vertical distance between the highest point in the first half and the lowest point in the second half is maximum). So, this last phase is mostly driven by the restoring potential elastic energy of the panel.

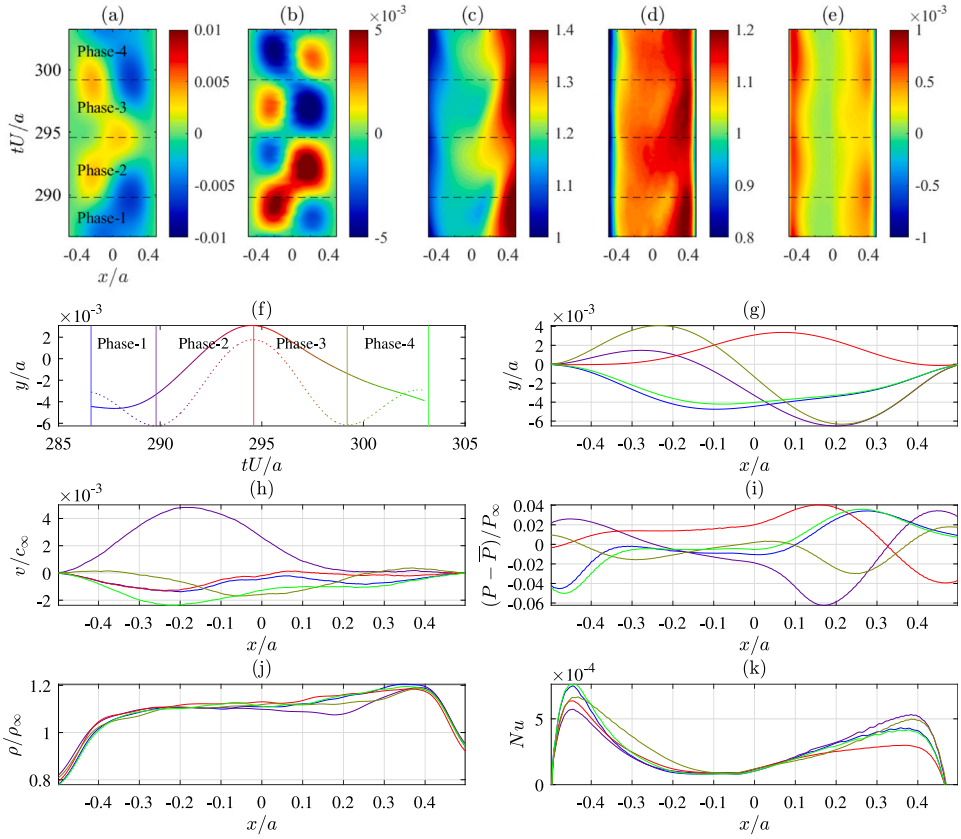

Fig. 27. x–t plot of (a) deflection, (b) y-velocity, (c) pressure, (d) density, and (e) non-dimensional heat-flux over a cycle for Case T-11c (where the heat is extracted through the bottom surface of the panel). (f) Mid-panel displacement (solid line) and 3/4th chord length displacement (dashed line), (g) displacement, (h) y-velocity, (i) pressure difference, (j) density, and (k) Nusselt number at $tU/a = 286.6, 289.8, 294.6, 299.2, 303.2$. (For interpretation of the references to color in this figure legend, the reader is referred to the web version of this article.)

Fig. 27(j) and (k) illustrate the fluid density and heat flux at the interface. At the position near the leading edge ($x/a = -0.45$) depicted in Fig. 27(k), the maximum heat flux occurs at $tU/a = 286.6$, coinciding with a locally concave shape of the panel. However, maximum heat transfer on the fore half of the panel happens at the beginning of phase-4 (Fig. 28 at $tU/a = 299.2$) where the panel reaches its maximum positive displacement. Since the separation bubble is shifted downstream and the panel is more exposed to the incoming fluid with higher temperature at this position, a higher rate of thermal interaction is observed between $x/a = -0.4$ to 0.1. On the other half of the panel, enhanced heat transfer is observed when the panel moves downward direction and brings fluid along with it. In Fig. 28 at $tU/a = 289.8$ and 299.2, the influx of lower density (i.e., higher temperature) fluid into the separation bubble causes the higher heat-flux on the second half of the panel.

3.2.3. *Effects of heating through the bottom wall*

To evaluate the impact of the heated bottom wall (Case T-11 h), the mid-panel deflection, top wall temperature, and heat flux are compared with the adiabatic wall case (Case T-11a) in Fig. 29(a) and (b). In the heated panel case, the panel deflection dampens at a faster rate compared to the adiabatic wall case and the plate settles at a higher deflection position in the middle of the panel compared to the adiabatic panel. This behavior is due to two main factors: thermal expansion and the heating effect on the adjacent fluid layer in the interaction zone. The thermal expansion (due to the higher temperature) contributes to the increased deflection. Furthermore, the effective elasticity of the solid decreases as the temperature increases. The lower stiffness is responsible for, the higher mean deflected position of the panel.Similarly, Daub et al. observed that heating reduces the stiffness of the structure for a prestressed panel which leads to larger deflection (Daub et al., 2022). However, later in their study, due to continued wind tunnel runs, the heated panel buckles against its frame with a drastic reduction in structural dynamics. Additionally, the heating of the adjacent fluid layer alters its properties, affecting the FSI behavior. The reduced density of the heated fluid results in lower momentum transfer from the flow to the structure. Consequently, the aerodynamic forces, influenced by the modification to the oblique shock action, along with the thermal dependency of the panel material, dictate the dynamic behavior here.

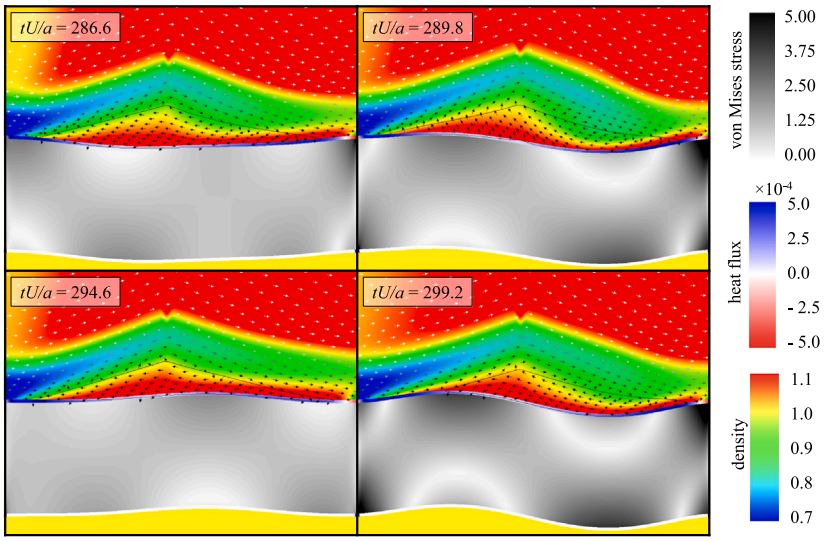

Fig. 28. Density contour of the flow field and von Mises stress contour in the solid snapshot at $tU/a = 286.6, 289.8, 294.6, 299.2$ (y-axis is enlarged 13 times for better visualization). The contour at the interface shows the heat flux. The solid black line shows the separation bubble. Arrows show the velocity vector (colored gray-scale by magnitude).

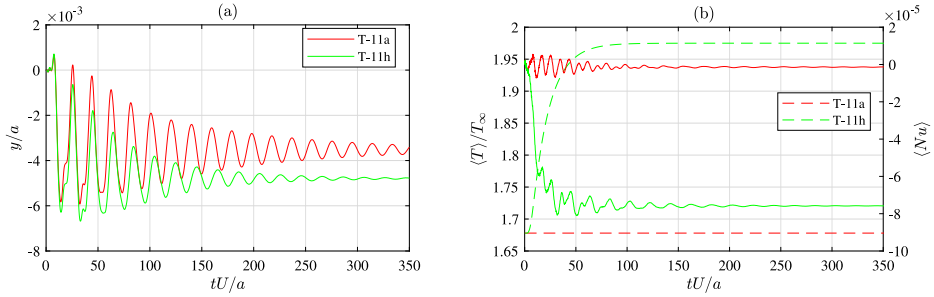

Fig. 29. (a) Mid-panel deflection, (b) spatially averaged wall temperature of the top surface (dashed line) and heat-flux (solid line) on the top wall for the Case T-11 h with heat supplied through the bottom of the panel.

4. Conclusion

This study investigates how aero-thermo-elastic interactions affect shock wave boundary layer interaction (SBLI) over an elastic structure with varying thermal conditions. Notably, this study is the first to comprehensively examine both thermally and dynamically two-way coupled FTSI systems in the context of SBLI.

We adopted an FSI modeling approach utilizing the higher-order sharp interface IBM. Initially, our simulations focused on analyzing the flow over a rigid panel under diverse conditions, including variations in wall temperatures, Reynolds numbers, and shock angles. The purpose was to determine the optimal flow parameters for FSI. Subsequently, we investigated SBLI over a compliant wall, considering different non-dimensional dynamic pressures and a fixed isothermal wall condition without thermal interaction with the solid. This allowed us to understand the combined effects of shock dynamics and panel flexibility. Moreover, additional simulations were carried out, incorporating various wall temperatures, to examine the collective roles of temperature and flexibility within the system. This comprehensive approach sought to elucidate the complex relationship between thermal effects and structural flexibility in SBLI.

In all tested cases where solid properties remain independent of temperature, we observe a damped sinusoidal oscillation of the panel. The observed oscillation arises from the interaction between the unsteady fluid force and the elastic force of the structure over an extended range of non-dimensional dynamic pressures studied in this research. The dominant mode of panel oscillation aligns with the structure's first mode of vibration when the cavity pressure is set to be similar to the incoming flow.

When the panel oscillates with a significant amplitude, on the same order of magnitude as the boundary layer thickness, we observe a pronounced reconfiguration effect on the separation bubble and shock structure. This interaction is characterized by a lock-in frequency coupling between the panel's deformation and the interaction zone. Higher frequency oscillation achieved by increasing Young's modulus of the panel does not cause much impact on the shape and size of the interaction region as the amplitude

of panel oscillation decreases with the high Young's modulus. When comparing the flexible cases to the rigid case, it was evident that the average surface pressure was elevated on the upstream side of the shock impingement point and decreased on the downstream side. The cavity pressure slightly modifies the frequency of the panel oscillation but mainly affects the deformation amplitude, which depends on Young's modulus as well. Initially, in this study, we quantified the influence of structural parameters and wall temperature on the decay rate, amplitude, and frequency of the panel oscillation. In the stable FSI system, both the panel stiffness and density significantly impact the frequency and decay rate of the self-excited decaying oscillation, while the final steady-state deflection of the panel depends on the stiffness and the cavity pressure.

On the other hand, the panel temperature predominantly impacts the size of the separation bubble. Lower temperatures lead to higher gradients in the shear layers along with a simultaneous reduction in the size of the bubble and consequently make the interaction region more unsteady. The relative size of the separation bubble with respect to the panel length is a key parameter to predict the effect of the oscillating panel on the flow field.

The thermal dependency of the structural properties significantly impacts the dynamics of the panel and could introduce new response modes. Depending on the panel temperature, the FSI system shows stable or oscillatory behavior. The effect of both heating and cooling has been evaluated for the fully-coupled FSI system. When panel stiffness changes due to reduced temperature, a stable decaying sinusoidal oscillation can transform into a limit-cycle oscillation. This transformation is associated with a simultaneous mode switch between the vibrational first and second modes of deformation of the panel. The interplay between temperature and structural properties thus was identified to govern the behavior of the FSI system.

Our research indicates that the interaction between the compliant panel and thermal conditions can significantly alter the oscillatory behavior of the panel, surpassing the influence of each factor in isolation. Unexpectedly, although the separate impacts of surface flexibility and applied thermal conditions on the inner surface of the panel appear to be minimal, the dynamic response of the panel experiences a significantly greater modification due to the thermo-elastic coupling within the system. This multiphysics interaction mode may render the system more vulnerable to fatigue-induced damage. Given the significant surface heating that occurs at the shock location in high-speed flows, it could be critical to employ a specialized thermal protection system beneath the panel (Uyanna and Najafi, 2020). Various strategies, both active and passive, have been proposed to mitigate excess heat, including the heat sink and heat pipes, which can induce substantial thermo-elastic coupling across the panel. This study highlights the potential unforeseen response mode of the panel in these conditions contingent on its thermal and thermo-elastic characteristics. Further research is necessary to characterize these potentially detrimental response modes and to establish guidelines for their prevention during the thermal and structural design phases of high-speed air vehicles.

Besides, this article supplements the limited literature on FTSI of SBLI for the laminar/turbulent boundary layer. Several similarities can be identified through comparisons with other studies on laminar/turbulent SBLI for rigid/flexible panels that are consistent with the findings in our study e.g. the dependency of the length and size of the separation bubble on the boundary layer, Reynolds number, wall temperature; impact of heating and cooling on the stiffness of the solid and the corresponding effect on the deflection. In experiments, the panel often buckles to a concave/convex shape and gets locked in its first mode shape if the panel thickness is very small and then oscillates around that position with a substantial reduction in structural dynamics. In the current study, this complex response mode is systematically suppressed for fixed–fixed side wall boundary conditions with a relatively thicker panel to ensure a more canonical configuration. However, similar panel buckling response modes have been observed for the pinned-pinned side wall boundary conditions and modified slow and fast response modes. The multiple timescale dynamics of such configurations will be studied in the future.

Fluid–structural–thermal interactions for high-speed flow are inherently complex and non-linear. Several influential parameters, including cavity pressure, wall temperature, Young's modulus, and thermal expansion, modify the effective excitation of shock-induced fluttering. Our future goal is to extend the fully coupled algorithm to explore the identified influential parameters in the 3D domain and to investigate the three-dimensional behavior of the interaction zone.

CRediT authorship contribution statement

Al Shahriar: Conceptualization, Methodology, Software, Validation, Formal analysis, Investigation, Writing – original draft, Writing – review & editing, Visualization. **Kourosh Shoele:** Conceptualization, Methodology, Formal analysis, Writing – original draft, Writing – review & editing, Resources, Supervision, Funding acquisition.

Declaration of competing interest

The authors declare the following financial interests/personal relationships which may be considered as potential competing interests: Kourosh Shoele, reports financial support was provided by The Defense Advanced Research Projects Agency.

Data availability

Data will be made available on request.

Acknowledgments

This study is supported by the Defense Advanced Research Projects Agency, United States, Grant number D19AP00035. The authors also acknowledge the Research Computing Center at Florida State University, United States made computational resources available for conducting the research reported in this paper.

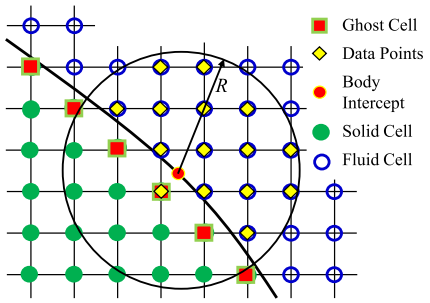

Fig. A.30. Graphical representation of higher-order sharp interface IBM.

Appendix A. Higher-order immersed boundary method

A higher-order sharp interface IBM is utilized for the fluid–structure coupling. In this method, the discretized flow equations are modified near the interfaces to enforce the interface conditions at the interface of fluid and solid (Kajishima and Taira, 2016). The closest fluid Eulerian node to the interface inside the solid domain is identified and tagged as a ghost node for the flow field. The normal drawn from the ghost cells intercepts the boundary at body-intercept points. The imposed boundary conditions as the body-intercepted points are expressed using interpolation of nearby flow variables. In the current study, to increase the order of accuracy, a weighted least-square error minimization method based on a higher-order approximate polynomial has been employed (Seo and Mittal, 2011). Fig. A.30 provides a visual description of this procedure. The solid black line represents the immersed boundary. Green solid circles and the ghost points (solid red squares with green boundaries) are the grid points inside the body and yellow diamonds are the grid points used for formulating the weighted least-square error minimization method. Following Seo and Mittal (2011), a generic variable $\phi(\mathbf{x})$ is approximated in the vicinity of the body-intercept point $\boldsymbol{x}_{BI} = (x_{BI}, y_{BI})^T$ with a Nth-order polynomial representation, as follows:

$$\phi(\boldsymbol{x}) \approx \sum_{i=0}^{N}\sum_{j=0}^{N}\sum_{k=0}^{N} \mathbf{C}_{ijk}(x')^i(y')^j \tag{A.1}$$

where $x' = x - x_{BI}, y' = y - y_{BI}$ and $\mathbf{C}_{ij}$ are the unknown coefficients. A circular (2D) region (of radius R) around the body-intercept point, see Fig. A.30, is interrogated to relate the coefficients of C_{ij} to the value of the ghost point and the reaming the $M-1$ data points in the fluid region. The solution to the least-square error problem is,

$$\mathbf{C} = (\mathbf{WV})^{+}\mathbf{W}\phi \tag{A.2}$$

where superscript '+' denotes the pseudo-inverse. The weights ($\mathbf{W}$) is defined as,

$$\mathbf{W} = \begin{bmatrix} W_0 & & \\ & \ddots & \\ & & W_{M-1} \end{bmatrix} \tag{A.3}$$

and Vandermonde matrix ($\mathbf{V}$) is,

$$\mathbf{V} = \begin{bmatrix} 1 & x'_0 & y'_0 & {x'_0}^2 & {y'_0}^2 & \cdots \\ 1 & x'_1 & y'_1 & {x'_1}^2 & {y'_1}^2 & \cdots \\ \vdots & \vdots & \vdots & \vdots & \vdots & \ddots \\ 1 & x'_{M-1} & y'_{M-1} & {x'_{M-1}}^2 & {y'_{M-1}}^2 & \cdots \end{bmatrix} \tag{A.4}$$

Here, (x'_0, y'_0) is the ghost point associated with $\boldsymbol{x}_{BI}$ and V is a $(M \times L)$ matrix where L is the number of coefficients needed for the reconstruction of an Eulerian variable near the interface. In the current study, $L = 10$ is selected to reach a third-order accuracy near the interface. The weighting matrix is defined as

$$\mathbf{W}_i = \frac{1}{2}(1 + \cos(\pi \frac{d_i}{R})), \quad d_i = \sqrt{x'_i + y'_i} \tag{A.5}$$

The interpolation radius R is selected to ensure a well-posedness condition. With a simplified notation of $\mathbf{A} = \mathbf{WV}^{+}\mathbf{W}$, the equation can be written for the ghost points for the Dirichlet boundary condition at the immersed surface as,

$$\phi_{GP} = C_{\text{Dir}}\left[\phi(\boldsymbol{x}_{BI}) - \sum_{m=2}^{M} \mathbf{A}(1,m)\cdot\phi(\boldsymbol{x}_m)\right], \qquad C_{\text{Dir}} = \frac{1}{\mathbf{A}(1,1)} \tag{A.6}$$

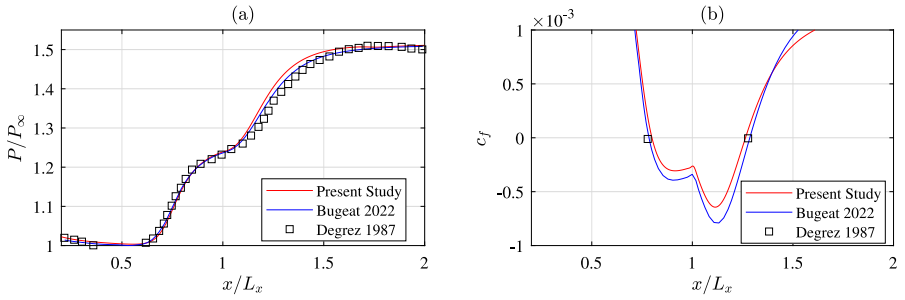

Fig. B.31. (a) Pressure and (b) skin-friction coefficient on the surface compared against CFD and experimental results. L_x is the distance between the leading edge and the shock impingement point.

A similar relation can be obtained for the Neumann boundary condition as,

$$\phi_{GP} = C_{\text{Nue}} \left[\phi_n(\boldsymbol{x}_{BI}) - \sum_{m=2}^{M} \hat{n} \cdot \phi(\boldsymbol{x}_m) \cdot (\mathbf{A}(2,m)\hat{i} + \mathbf{A}(3,m)\hat{j}) \right], \qquad C_{\text{Nue}} = \frac{1}{\hat{\mathbf{n}} \cdot (\mathbf{A}(2,1)\hat{i} + \mathbf{A}(3,1)\hat{j})} \tag{A.7}$$

where $\hat{\mathbf{n}}$ is the normal to the interface and $\phi_n(\mathbf{x}_{BI})$ is related to the imposed flux on the surface. Eqs. (A.6) and (A.7) can be employed to represent different temperature conditions at the interfaces.

Appendix B. Validation cases

B.1. Flow solver validation

B.1.1. Validation of laminar SBLI over rigid surface

In order to validate the flow solver, SBLI over the rigid surface has been compared against the computational fluid dynamic results of Bugeat et al. (2022) and experimental results of Degrez et al. (1987) as shown in Fig. B.31. For this setup, the Mach number, shock angle, and Reynolds number (based on the streamwise length from the leading edge to the shock impingement location) are $Ma = 2.15$, $\beta = 30.8°$ (corresponding to a pressure jump $P_3/P_\infty = 1.55$) and $Re_x = 0.96 \times 10^5$, respectively. Both the surface pressure in Fig. B.31(a) and separation bubble size in the skin-friction curve in Fig. B.31(b) show good agreement with the CFD and experimental results.

B.1.2. Validation for flow over a cylinder

The computational model has been validated for several canonical test cases, including subsonic and supersonic flows over a circular cylinder. Non-uniform finer grids are employed to reach higher resolution around the cylinder. At a low Reynolds number, the supersonic flow is steady with an elongated downstream wake as shown in Fig. B.32(a), and a detached bow shock wave is formed in front of the cylinder. The standoff location of the detached bow shock is compared well with the results in Shahriar (2015), Mittal (1998). As an example, the density contour lines (colored) on the upper half with 30 levels are compared with the previously reported contour lines (black) in Mittal (1998). The force estimation from our model also agrees well with the literature. The drag coefficient of the case with $Ma = 2$ and $Re_D = 2000$ shown in Fig. B.32(a) is 1.41 in our simulation, close to the reported value 1.45 in Gowen and Perkins (1953). Overall, a good comparison is observed between our prediction and reported results for $Ma = 2$ and $Re_D = 50$ and 2000.

Further validations have been provided for the low Mach number flows. The drag and lift variation of flow over a cylinder at $Re = 3900$ is shown in Fig. B.33(a). The mean pressure distribution around the cylinder at $Re = 3900$ is compared with the reported values in Fig. B.33(b) where a good agreement is found. Table B.7 includes the comparison between the current method and other studies for the lift and drag coefficients as well as the Strouhal number ($St = fD/U$) of an incompressible flow over a cylinder at different Reynolds numbers. Here, the incompressibility is achieved by choosing lower values of flow speed ($Ma = 0.2$) in the compressible solver and turning off the artificial viscosity condition.

B.2. Structural solver validation

B.2.1. Dynamic behaviors

The flexible solid is discretized with uniform quadrilateral meshes. Different mesh resolutions have been tested with the non-linear FEM solver and the final setup with 18 grids in the thickness direction and 331 grids in the longitudinal direction is selected. For standalone validation of the structural solver, at first, the natural vibration mode shapes and frequencies are calculated from the

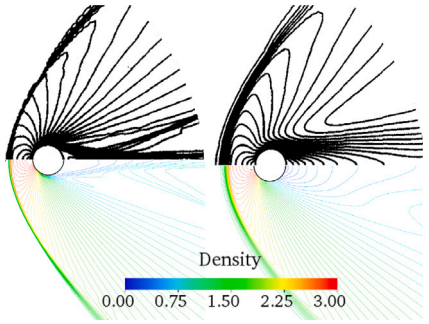

Fig. B.32. Density contour plot for Mach 2 and $Re_D = 2000$ and $Re_D = 50$ flow. Black contour lines are the results reported in Mittal (1998). (For interpretation of the references to color in this figure legend, the reader is referred to the web version of this article.)

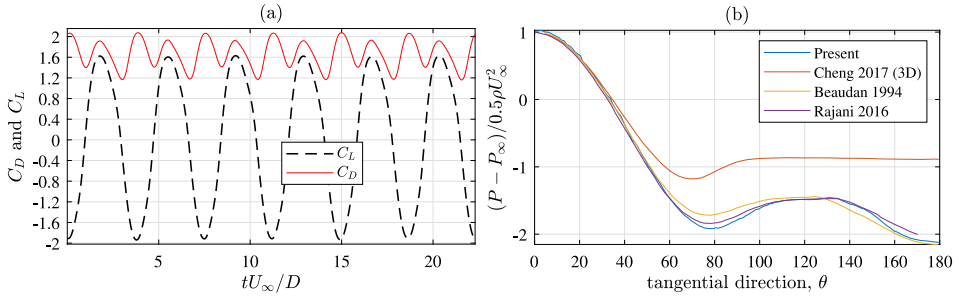

Fig. B.33. (a) Time history of drag (C_D) and lift (C_L) coefficient for $Re_D = 3900$, (b) Time average pressure on the surface of the cylinder for $Re_D = 3900$ and comparing with Cheng et al. (2017), Beaudan and Moin (1994) and Rajani et al. (2016).

Table B.7
Comparison of Strouhal number (St), an average of drag coefficient ($\overline{C}_D$), RMS of lift coefficient (C'_L) for an incompressible flow over a cylinder at different Reynolds number.

$Re_D = 100$	$\overline{C}_D$	$\overline{C}_{D,S}$	C'_L	St	$Re_D = 300$	$\overline{C}_D$	$\overline{C}_{D,S}$	C'_L	St
Posdziech and Grundmann (2007)	1.33	–	0.23	0.16	Rajani et al. (2009)	1.37	–	0.60	0.21
Rajani et al. (2009)	1.34	–	0.18	0.16	Mittal and Balachandar (1997)	1.38	–	0.65	0.21
Qu et al. (2013)	1.32	–	0.23	0.17	Henderson (1995)	1.40	0.21		
Present	1.36	0.31	0.20	0.16	Present	1.39	0.19	0.62	0.21
$Re_D = 1000$					$Re_D = 3900$				
Henderson (1995)	1.52	0.13	–	–	Beaudan and Moin (1994)	1.74	–	–	0.26
Present	1.50	0.09	1.01	0.23	Present	1.70	0.04	1.12	0.27

eigenvalue analysis of the finite-element model, and the first three frequencies are shown by the dashed vertical line in Fig. B.34. To validate the dynamic non-linear solver, the response of the structural system to an impulse force has been evaluated. The impulse force is applied at the 3/4th chord length of the panel for 5% of the fundamental period of oscillation which is obtained by the following equation. The panel's motion at 0.25, 0.5, and 0.75 chord lengths shows the first three natural frequencies of the system in Fig. B.34. The theoretical value of the panel frequency from the beam theory for a fixed–fixed beam is

$$\omega_0 = \frac{22.4}{2\pi}\sqrt{\frac{Eh^2}{12(1-\nu^2)\rho_s a^4}} \tag{B.1}$$

For this setup, the theoretical frequency ($\omega_0 a/U$) is 0.0644 which is very close (2.2% error) to the first dominant frequency obtained in Fig. B.34. In conclusion, the non-linear structural solver can capture the dynamic modes of the panel oscillation very accurately.

B.2.2. Thermally coupled behaviors

In order to validate our coupled thermal and structural system, a benchmark test was conducted on a pinned-pinned beam. In this test, a temporally increasing (but constant in the longitudinal direction) thermal load was applied to the top surface by gradually increasing the temperature, while the bottom surface was kept constant at a neutral temperature (the stress-free temperature where the panel neither experience tension nor compression). The non-dimensional thermal conductivity ($\kappa_s T_\infty/\rho_\infty U^3 a$), specific heat ($C_{p_s} T_\infty/U^2$), and thermal expansion coefficient (αT_∞) were set to values of 0.52, 2.2, and 3.3×10^{-3}, respectively. The applied

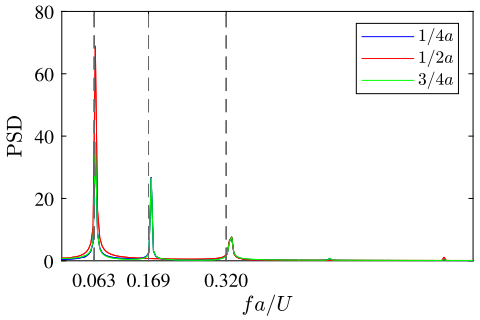

Fig. B.34. Natural frequency of the structural system. Dashed vertical lines show frequencies obtained by eigenvalue analysis.

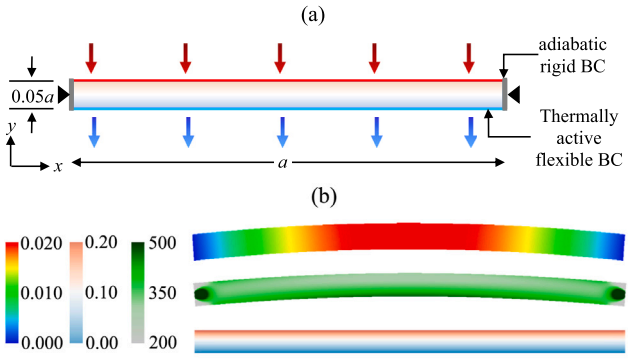

Fig. B.35. (a) Schematic of the coupled structural system, (b) y-displacement, von Misses stress, and temperature for thermally and structurally coupled panel. Deformation has been amplified 10 times for clarity.

thermal load on the surface of the panel generates corresponding stresses within the panel, resulting in thermal buckling or thermal instability, as depicted in Fig. B.35. As expected, stresses were concentrated on the pinned location of the beam.

B.3. Validation of fully-coupled FSI algorithm

In this section, a validation study has been conducted to verify the fully-coupled FSI algorithm. The authors conduct a similar study reported in Li et al. (2019) for SBLI over a flexible panel. The validation study has been conducted for $Re_a = 120,000$ (Reynolds number based on panel length), $\delta_{LE} = 0.015a$ (boundary layer thickness at the leading edge of the flexible panel), $P_3/P_1 = 1.4$ (mean pressure along the panel length by the inviscid oblique shock reflection), $P_c/P_\infty = 1.2$ (cavity pressure), shock impingement location $(x/a) = 0.5$ (mid-panel), $M^* = 0.1$ (mass ratio), $\lambda = 875$ (non-dimensional dynamic pressure), $\nu_s = 0.3$ (Poisson ratio), pinned-pinned panel and $h/a = 0.002$ (panel aspect ratio). The domain is discretized by 1025×159 grids with uniform streamwise grids and stretched wall-normal grids. Near-wall grid size is $0.0003a$ and the time step $(\Delta tU/a)$ is 0.0002.

The time series data of the deflection at 3/4th chord length shows a limit cycle oscillation in Fig. B.36(a). The amplitude decreases initially within a few oscillations and then increases until reaches a limit cycle oscillation. The same behavior was observed for the deflection at 3/4th chord length in Li et al. (2019). Fig. B.36(b) compares the time-averaged deflection profile and surface pressure for our current algorithm and literature. The slight difference between results might originate from the fortuitous shock originating from the zone where the inflow compressible boundary layer is imposed. In Li et al. (2019), the pressure contour plot shows that the leading edge inflow shock interacts with the original shock imposed at the top boundary. This shock also modifies the surface pressure downstream. Whereas, in the current study, the artificial inflow shock is very weak and almost imperceptible.

Appendix C. Comparison with the piston theory

In Gogulapati et al. (2015), the motion of the compliant panel due to the fluttering behavior and the turbulent boundary layer is modeled by augmenting the mean flow solution using suitable terms. The surface pressure has been constituted as local piston theory pressure, cavity pressure, and fluctuating pressure for turbulent flow.

$$P(x,t) = P_{PT}(x,t) + P_{TBL}(x,t) + P_c \tag{C.1}$$

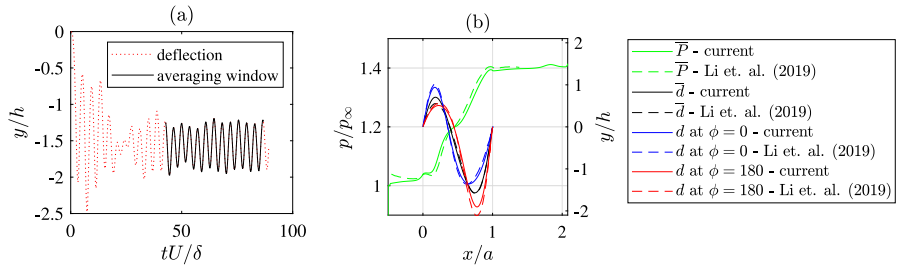

Fig. B.36. (a) Deflection at 3/4th chord length. (b) Mean deflection, mean pressure, and deflection profile at the peak and valley of the time-series deflection at $x/a = 3/4$. The black curve of the oscillation shows the averaging window.

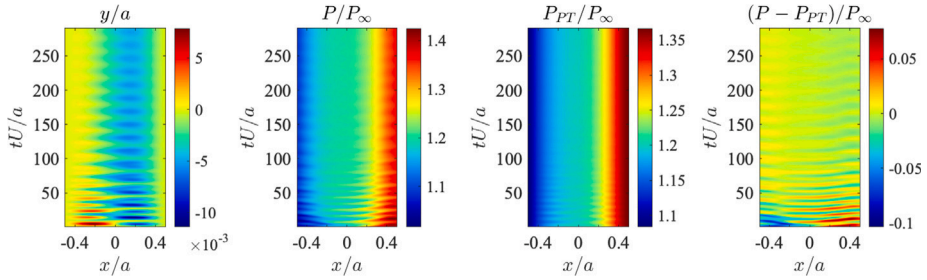

Fig. C.37. Comparison of results between fully coupled FTSI simulation and piston theory: x–t plot of (a) deflection, (b) FTSI surface pressure, (c) piston theory pressure, and (d) difference between the pressure.

Then, the piston theory pressure is formulated using the following equation derived from classical piston theory along with the kriging surrogates (P_{loc}, a_{loc}) that are constructed from a series of steady-state CFD flow responses.

$$P_{PT}(x,t) = P_{loc}(x,t)\left[1 + \gamma \frac{\dot{w}}{a_{loc}(x,t)}\right] \tag{C.2}$$

For our setup, based on piston theory, we construct the pressure from the recorded surface motion during the simulation. The panel motion ($\dot{w}$) and surrogates (P_{loc}, a_{loc}) were recorded during the simulation and the term P_{TBL} is ignored. The comparison of this variant of piston theory with the full-coupled FSI system (Case T-11a) is illustrated in Fig. C.37.

Appendix D. Supplementary data

Supplementary material related to this article can be found online at https://doi.org/10.1016/j.jfluidstructs.2023.104047.

References

Agostini, L., Larchevêque, L., Dupont, P., Debiève, J.-F., Dussauge, J.-P., 2012. Zones of influence and shock motion in a shock/boundary-layer interaction. AIAA J. 50 (6), 1377–1387.

Aubard, G., Gloerfelt, X., Robinet, J.-C., 2013. Large-eddy simulation of broadband unsteadiness in a shock/boundary-layer interaction. AIAA J. 51 (10), 2395–2409.

Babinsky, H., Harvey, J.K., 2011. Shock Wave-Boundary-Layer Interactions, Vol. 32. Cambridge University Press.

Beaudan, P., Moin, P., 1994. Numerical Experiments on the Flow Past a Circular Cylinder at Sub-Critical Reynolds Number. Tech. Rep., Stanford Univ CA Thermosciences Div.

Benay, R., Chanetz, B., Mangin, B., Vandomme, L., Perraud, J., 2006. Shock wave transitional boundary-layer interactions in hypersonic flow. AIAA J. 44 (6), 1243–1254.

Bernardini, M., Asproulias, I., Larsson, J., Pirozzoli, S., Grasso, F., 2016. Heat transfer and wall temperature effects in shock wave turbulent boundary layer interactions. Phys. Rev. Fluids 1 (8), 084403.

Bhardwaj, R., Mittal, R., 2012. Benchmarking a coupled immersed-boundary-finite-element solver for large-scale flow-induced deformation. AIAA J. 50 (7), 1638–1642.

Bhardwaj, R., Ziegler, K., Seo, J.H., Ramesh, K., Nguyen, T.D., 2014. A computational model of blast loading on the human eye. Biomech. Model. Mechanobiol. 13 (1), 123–140.

Bodony, D.J., 2006. Analysis of sponge zones for computational fluid mechanics. J. Comput. Phys. 212 (2), 681–702.

Brouwer, K.R., Gogulapati, A., McNamara, J.J., 2017. Interplay of surface deformation and shock-induced separation in shock/boundary-layer interactions. AIAA J. 1–16.

Bugeat, B., Robinet, J.-C., Chassaing, J.-C., Sagaut, P., 2022. Low-frequency resolvent analysis of the laminar oblique shock wave/boundary layer interaction. J. Fluid Mech. 942, A43.

Chapman, S., Cowling, T.G., 1990. The Mathematical Theory of Non-Uniform Gases: An Account of the Kinetic Theory of Viscosity, Thermal Conduction and Diffusion in Gases. Cambridge University Press.

Cheng, W., Pullin, D., Samtaney, R., Zhang, W., Gao, W., 2017. Large-eddy simulation of flow over a cylinder with: a skin-friction perspective. J. Fluid Mech. 820, 121–158.
Cook, A.W., Cabot, W.H., 2004. A high-wavenumber viscosity for high-resolution numerical methods. J. Comput. Phys. 195 (2), 594–601.
Cook, A.W., Cabot, W.H., 2005. Hyperviscosity for shock-turbulence interactions. J. Comput. Phys. 203 (2), 379–385.
Culler, A.J., 2010. Coupled Fluid-Thermal-Structural Modeling and Analysis of Hypersonic Flight Vehicle Structures (Ph.D. thesis). The Ohio State University.
Culler, A.J., McNamara, J.J., 2010. Studies on fluid-thermal-structural coupling for aerothermoelasticity in hypersonic flow. AIAA J. 48 (8), 1721–1738.
Culler, A., McNamara, J., 2011. Fluid-thermal-structural modeling and analysis of hypersonic structures under combined loading. In: 52nd AIAA/ASME/ASCE/AHS/ASC Structures, Structural Dynamics and Materials Conference 19th AIAA/ASME/AHS Adaptive Structures Conference 13t. p. 1965.
D'Aguanno, A., Quesada Allerhand, P., Schrijer, F., van Oudheusden, B., 2023. Characterization of shock-induced panel flutter with simultaneous use of dic and piv. Exp. Fluids 64 (1), 15.
Daub, D., Willems, S., Gülhan, A., 2022. Experiments on aerothermoelastic fluid–structure interaction in hypersonic flow. J. Sound Vib. 116714.
Degrez, G., Boccadoro, C., Wendt, J., 1987. The interaction of an oblique shock wave with a laminar boundary layer revisited. an experimental and numerical study. J. Fluid Mech. 177, 247–263.
Delery, J.M., 1985. Shock wave/turbulent boundary layer interaction and its control. Prog. Aerosp. Sci. 22 (4), 209–280.
Délery, J., Dussauge, J.-P., 2009. Some physical aspects of shock wave/boundary layer interactions. Shock Waves 19 (6), 453.
Dolling, D.S., 2001. Fifty years of shock-wave/boundary-layer interaction research: what next? AIAA J. 39 (8), 1517–1531.
Dowell, E.H., Hall, K.C., 2001. Modeling of fluid–structure interaction. Annu. Rev. Fluid Mech. 33 (1), 445–490.
Fang, J., Yao, Y., Li, Z., Lu, L., 2014. Investigation of low-dissipation monotonicity-preserving scheme for direct numerical simulation of compressible turbulent flows. Comput. & Fluids 104, 55–72.
Fiorina, B., Lele, S.K., 2007. An artificial nonlinear diffusivity method for supersonic reacting flows with shocks. J. Comput. Phys. 222 (1), 246–264.
Freydin, M., Dowell, E.H., Spottswood, S.M., Perez, R.A., 2021. Nonlinear dynamics and flutter of plate and cavity in response to supersonic wind tunnel start. Nonlinear Dynam. 103 (4), 3019–3036.
Freydin, M., Dowell, E.H., Varigonda, S.V., Narayanaswamy, V., 2022. Response of a plate with piezoelectric elements to turbulent pressure fluctuation in supersonic flow. J. Fluids Struct. 114, 103696.
Gaitonde, D.V., Adler, M.C., 2022. Dynamics of three-dimensional shock-wave/boundary-layer interactions. Annu. Rev. Fluid Mech. 55.
Ganapathisubramani, B., Clemens, N., Dolling, D., 2007. Effects of upstream boundary layer on the unsteadiness of shock-induced separation. J. Fluid Mech. 585, 369–394.
Gao, M., Appel, D., Beck, A., Munz, C.-D., 2023. A high-order fluid–structure interaction framework with application to shock-wave/turbulent boundary-layer interaction over an elastic panel. J. Fluids Struct. 121, 103950.
Garnier, E., 2009. Stimulated detached eddy simulation of three-dimensional shock/boundary layer interaction. Shock Waves 19 (6), 479.
Gogulapati, A., Deshmukh, R., McNamara, J.J., Vyas, V., Wang, X., Mignolet, M.P., Beberniss, T., Spottswood, S.M., Eason, T., 2015. Response of a panel to shock impingement: Modeling and comparison with experiments-part 2. In: 56th AIAA/ASCE/AHS/ASC Structures, Structural Dynamics, and Materials Conference. p. 0685.
Gottlieb, S., Shu, C.-W., 1998. Total variation diminishing Runge–Kutta schemes. Math. Comput. 67 (221), 73–85.
Gowen, F.E., Perkins, E.W., 1953. Drag of Circular Cylinders for a Wide Range of Reynolds Numbers and Mach Numbers. Tech. Rep. TN-2960, NACA.
Grilli, M., Schmid, P.J., Hickel, S., Adams, N.A., 2012. Analysis of unsteady behaviour in shockwave turbulent boundary layer interaction. J. Fluid Mech. 700, 16–28.
Gs, S., Dwivedi, A., Candler, G.V., Nichols, J.W., 2017. Global linear stability analysis of high-speed flows on compression ramps. In: 47th AIAA Fluid Dynamics Conference. p. 3455.
Guiho, F., Alizard, F., Robinet, J.-C., 2016. Instabilities in oblique shock wave/laminar boundary-layer interactions. J. Fluid Mech. 789, 1–35.
Hayashi, M., Sakurai, A., Aso, S., 1986. Measurement of Heat-Transfer Coefficients in Shock Wave-Turbulent Boundary Layer Interaction Regions with a Multi-Layered Thin Film Heat Transfer Gauge, Transl. into ENGLISH from Memoirs of the Faculty of Engineering of Kyushu Univ. Technology Reports (Japan), V. 57, Aug. 1984. pp. 455–462.
Heil, M., Hazel, A.L., Boyle, J., 2008. Solvers for large-displacement fluid–structure interaction problems: segregated versus monolithic approaches. Comput. Mech. 43 (1), 91–101.
Henderson, R.D., 1995. Details of the drag curve near the onset of vortex shedding. Phys. Fluids 7 (9), 2102–2104.
Hilber, H.M., Hughes, T.J., Taylor, R.L., 1977. Improved numerical dissipation for time integration algorithms in structural dynamics. Earthq. Eng. Struct. Dyn. 5 (3), 283–292.
Hosters, N., Klaus, M., Schieffer, G., Behr, M., Reimerdes, H.-G., 2013. Towards aerothermoelastic simulations of supersonic flow through nozzles. Prog. Propuls. Phys. 4, 637–654.
Hou, G., Wang, J., Layton, A., 2012. Numerical methods for fluid–structure interaction—a review. Commun. Comput. Phys. 12 (2), 337–377.
Jaunet, V., Debieve, J., Dupont, P., 2014. Length scales and time scales of a heated shock-wave/boundary-layer interaction. AIAA J. 52 (11), 2524–2532.
Kajishima, T., Taira, K., 2016. Computational Fluid Dynamics: Incompressible Turbulent Flows. Springer.
Katzer, E., 1989. On the lengthscales of laminar shock/boundary-layer interaction. J. Fluid Mech. 206, 477–496.
Kawai, S., Lele, S.K., 2007. Localized Artificial Viscosity and Diffusivity Scheme for Capturing Discontinuities on Curvilinear and Anisotropic Meshes. Center for Turbulence Research Annual Research Briefs.
Lele, S.K., 1992. Compact finite difference schemes with spectral-like resolution. J. Comput. Phys. 103 (1), 16–42.
Li, Y., Luo, H., Chen, X., Xu, J., 2019. Laminar boundary layer separation over a fluttering panel induced by an oblique shock wave. J. Fluids Struct. 90, 90–109.
Mani, A., 2010. On the Reflectivity of Sponge Zones in Compressible Flow Simulations. Center for Turbulence Research, Annual Research Briefs, pp. 117–133.
Mittal, S., 1998. Finite element computation of unsteady viscous compressible flows. Comput. Methods Appl. Mech. Engrg. 157 (1–2), 151–175.
Mittal, R., Balachandar, S., 1997. On the inclusion of three-dimensional effects in simulations of two-dimensional bluff-body wake flows. In: ASME Fluids Engineering Division Summer Meeting. pp. 1–6.
Mittal, R., Dong, H., Bozkurttas, M., Najjar, F., Vargas, A., von Loebbecke, A., 2008. A versatile sharp interface immersed boundary method for incompressible flows with complex boundaries. J. Comput. Phys. 227 (10), 4825–4852.
Nichols, J.W., Larsson, J., Bernardini, M., Pirozzoli, S., 2017. Stability and modal analysis of shock/boundary layer interactions. Theor. Comput. Fluid Dyn. 31 (1), 33–50.
Niessen, S., 2017. Biglobal stability analysis: Laminar shock-wave/boundary-layer interactions.
Ostoich, C.M., Bodony, D.J., Geubelle, P.H., 2013. Interaction of a mach 2.25 turbulent boundary layer with a fluttering panel using direct numerical simulation. Phys. Fluids 25 (11), 110806.
Pagella, A., Rist, U., Wagner, S., 2002. Numerical investigations of small-amplitude disturbances in a boundary layer with impinging shock wave at ma=4.8. Phys. Fluids 14 (7), 2088–2101.
Pasquariello, V., 2018. Analysis and Control of Shock-Wave Turbulent Boundary-Layer Interactions on Rigid and Flexible Walls (Ph.D. thesis). University Library of the Technical University of Munich.
Pasquariello, V., Grilli, M., Hickel, S., Adams, N.A., 2014. Large-eddy simulation of passive shock-wave/boundary-layer interaction control. Int. J. Heat Fluid Flow 49, 116–127.

Piponniau, S., Dussauge, J.-P., Debieve, J.-F., Dupont, P., 2009. A simple model for low-frequency unsteadiness in shock-induced separation. J. Fluid Mech. 629, 87–108.
Pirozzoli, S., Grasso, F., 2006. Direct numerical simulation of impinging shock wave/turbulent boundary layer interaction at m=2.25. Phys. Fluids 18 (6), 065113.
Posdziech, O., Grundmann, R., 2007. A systematic approach to the numerical calculation of fundamental quantities of the two-dimensional flow over a circular cylinder. J. Fluids Struct. 23 (3), 479–499.
Priebe, S., Martín, M.P., 2012. Low-frequency unsteadiness in shock wave–turbulent boundary layer interaction. J. Fluid Mech. 699, 1–49.
Purwar, A., Mahapatra, D.R., Thakor, N., Priyamvada, K., Mukherjee, R., 2017. A methodology for coupled thermal-structural analysis and structural design of scramjet combustor. In: 30th International Symposium on Shock Waves 1. Springer, pp. 245–250.
Qu, L., Norberg, C., Davidson, L., Peng, S.-H., Wang, F., 2013. Quantitative numerical analysis of flow past a circular cylinder at Reynolds number between 50 and 200. J. Fluids Struct. 39, 347–370.
Rajani, B., Kandasamy, A., Majumdar, S., 2009. Numerical simulation of laminar flow past a circular cylinder. Appl. Math. Model. 33 (3), 1228–1247.
Rajani, B., Kandasamy, A., Majumdar, S., 2016. Les of flow past circular cylinder at re=3900. J. Appl. Fluid Mech. 9 (3).
Robinet, J.-C., 2007. Bifurcations in shock-wave/laminar-boundary-layer interaction: global instability approach. J. Fluid Mech. 579, 85–112.
Sander, G., Bon, C., Geradin, M., 1973. Finite element analysis of supersonic panel flutter. Internat. J. Numer. Methods Engrg. 7 (3), 379–394.
Sandham, N., Schülein, E., Wagner, A., Willems, S., Steelant, J., 2014. Transitional shock-wave/boundary-layer interactions in hypersonic flow. J. Fluid Mech. 752, 349–382.
Sansica, A., Sandham, N., Hu, Z., 2014. Forced response of a laminar shock-induced separation bubble. Phys. Fluids 26 (9), 093601.
Seo, J.H., Mittal, R., 2011. A high-order immersed boundary method for acoustic wave scattering and low-mach number flow-induced sound in complex geometries. J. Comput. Phys. 230 (4), 1000–1019.
Shahriar, A., 2015. Study and Simulation of Inviscid Supersonic Flow over a Bluff Body. Department of Mechanical Engineering-Chittagong University of Engineering & Technology, Bangladesh.
Shahriar, A., Shoele, K., Kumar, R., 2018. Aero-thermo-elastic simulation of shock-boundary layer interaction over a compliant surface. In: AIAA Aviation Forum. p. 3398.
Shinde, V., McNamara, J., Gaitonde, D., 2022. Dynamic interaction between shock wave turbulent boundary layer and flexible panel. J. Fluids Struct. 113, 103660.
Shinde, V., McNamara, J.J., Gaitonde, D.V., Barnes, C.J., Visbal, M.R., 2018. Panel flutter induced by transitional shock wave boundary layer interaction. In: 2018 Fluid Dynamics Conference. p. 3548.
Spottswood, S.M., Beberniss, T.J., Eason, T.G., Perez, R.A., Donbar, J.M., Ehrhardt, D.A., Riley, Z.B., 2019. Exploring the response of a thin, flexible panel to shock-turbulent boundary-layer interactions. J. Sound Vib. 443, 74–89.
Thornton, E.A., 1992. Thermal structures-four decades of progress. J. Aircr. 29 (3), 485–498.
Touber, E., Sandham, N.D., 2009. Large-eddy simulation of low-frequency unsteadiness in a turbulent shock-induced separation bubble. Theor. Comput. Fluid Dyn. 23 (2), 79–107.
Uyanna, O., Najafi, H., 2020. Thermal protection systems for space vehicles: A review on technology development, current challenges and future prospects. Acta Astronaut. 176, 341–356.
Varigonda, S., Narayanaswamy, V., 2023. Fluid structure interactions generated by an oblique shock impinging on a thin elastic panel. J. Fluids Struct. 119, 103890.
Vasconcelos, P.B., McQuellin, L.P., Talluru, K.M., Neely, A.J., 2023. High-speed fluid–structure interactions on a compliant panel under shock impingement. AIAA J. 61 (3), 1077–1094.
Vedeneev, V.V., 2012. Panel flutter at low supersonic speeds. J. Fluids Struct. 29, 79–96.
Visbal, M., 2012. On the interaction of an oblique shock with a flexible panel. J. Fluids Struct. 30, 219–225.
Visbal, M., 2014. Viscous and inviscid interactions of an oblique shock with a flexible panel. J. Fluids Struct. 48, 27–45.
Volpiani, P.S., Bernardini, M., Larsson, J., 2018. Effects of a nonadiabatic wall on supersonic shock/boundary-layer interactions. Phys. Rev. Fluids 3 (8), 083401.
Volpiani, P.S., Bernardini, M., Larsson, J., 2020. Effects of a nonadiabatic wall on hypersonic shock/boundary-layer interactions. Phys. Rev. Fluids 5 (1), 014602.
White, F.M., Corfield, I., 2006. Viscous Fluid Flow, Vol. 3. McGraw-Hill New York.
Willems, S., Gülhan, A., Esser, B., 2013. Shock induced fluid–structure interaction on a flexible wall in supersonic turbulent flow. Prog. Flight Phys. 5, 285–308.
Wu, M., Martin, M.P., 2007. Direct numerical simulation of supersonic turbulent boundary layer over a compression ramp. AIAA J. 45 (4), 879–889.
Wu, M., Martin, M.P., 2008. Analysis of shock motion in shockwave and turbulent boundary layer interaction using direct numerical simulation data. J. Fluid Mech. 594, 71–83.
Zhou, H., Wang, G., Li, Q., Liu, Y., 2023. Numerical study on the nonlinear characteristics of shock-induced two-dimensional panel flutter in inviscid flow. J. Sound Vib. 117893.